Osteocytes as indicators of bone quality

Multiscale structure-composition characterisation of the bone-implant interface

Furqan Ali Shah

Department of Biomaterials
Institute of Clinical Sciences
Sahlgrenska Academy, University of Gothenburg

UNIVERSITY OF GOTHENBURG

Gothenburg 2017

Cover illustration: Laser-ablation of titanium results in the formation of globular features due to resolidifiation of metal with a highly ordered titanium dioxide on the surface. The image shows osteocytes in bone communicating with an osseointegrated implant surface via the lacuno-canalicular network. The structures have been revealed by sequential exposure of a resin embedded, explanted bone-implant specimen to mild acid and alkali solutions. Scanning electron microscopy (×10,000).

Osteocytes as indicators of bone quality

furqan.ali.shah@biomaterials.gu.se

ISBN 978-91-629-0260-5
http://hdl.handle.net/2077/52415

Printed in Gothenburg, Sweden 2017
Ineko AB

“The only thing that’s holding you back is the way you’re thinking.”

Steve Vai

ABSTRACT

By virtue of certain design features, bone anchored metal implants can be made to elicit a strong initial osteogenic response, i.e., the amount of bone formed. While quantitative differences are often lost at longer follow up times, do differences in the initial osteogenic response lead to long-term alterations in bone quality? This thesis investigates osseointegration in terms of bone quality, with an emphasis on the osteocyte lacuno-canalicular network (Ot.LCN) in relation to compositional and ultrastructural patterns observed at intermediate or late healing. A series of investigations was undertaken to study osteocyte lacunae on the forming bone surface (Paper I), hypermineralised lacunae of apoptotic osteocytes (Paper II), autogenous bone fragments found within healing sites (Paper III), bone formed adjacent to surface modified implants (Papers IV–VI), and bone formed within macroporous implants (Papers VII and VIII) using a range of analytical microscopy and complementary spectroscopic techniques. A directional relationship exists between the shape of the osteocyte lacuna and the underlying bone surface. The physico-chemical environment of the lacunar space is, however, different from the surrounding bone matrix, resulting in formation of a calcium phosphate phase more stable than apatite at lower pH, i.e., magnesium whitlockite. Connectivity between osteocytes within unintentionally generated autogenous bone fragments and *de novo* formed bone on their surface indicates a regenerative capacity of osteocytes. Laser-ablation creates a hierarchical micro- and nanotopography on titanium implants and enhances their biomechanical anchorage. Osteocytes attach directly to such surfaces, while mineralised collagen fibril organisation at bone-implant and bone-osteocyte interfaces is similar. More osteocytes are retained in the vicinity of Ti6Al4V surface as manufactured by electron beam melting than machined Ti6Al4V. In addition to cp-Ti and Ti6Al4V (ASTM F136), osteocytes also attach to CoCr (ASTM F75) thus indicating a favourable osteogenic response of a material generally considered inferior to Ti6Al4V. Therefore, osteocytes reveal vital information about bone quality and are important structural markers of osseointegration. Evaluation of the Ot.LCN can be extremely beneficial in characterising the bone response to materials intended for bone anchored, load bearing applications.

Keywords: 3D printing; apatite; biomaterials; biomineralisation; bone; bone quality; canaliculi; CoCr; collagen; electron beam melting; electron microscopy; implant; interface; in vivo; lacuna; micropetrosis; osseointegration; osteocyte; Raman spectroscopy; surface modification; Ti6Al4V; titanium; ultrastructure; whitlockite

SAMMANFATTNING PÅ SVENSKA

Osseointegrerade (benförankrade) metalliska implantat används i allt högre utsträckning inom tand- och sjukvården för att förankra proteser eller ersätta skadade anatomiska funktioner. Genom implantatdesign och ytmodifieringar så kan den initiala inläkningen påskyndas vilket resulterar i en ökad benmängd kring implantatet vid tidig fas. Vid längre uppföljningar så jämnas de tidiga skillnaderna i benmängd ut. Denna avhandling undersöker huruvida benkvaliteten också skiljer sig åt kring implantat av olika material eller ytmodifieringar och fokuserar mest på längre läktider då mängden benvävnad inte skiljer sig åt. Genom att studera hur osteocyter (benceller inbäddade i lakuner i vävnaden) är organiserade och sammankopplade i relation till benets lokala struktur och sammansättning återfås ett mått på dess kvalitet. I en serie undersökningar har osteocytlakuner på benbildningsytan (Studie I), återförslutningen av lakunen efter cellapoptos (Studie II) och relationen mellan osteocyter i nybildat och gammalt ben (Studie III) studerats. Vidare har benbildning kring ytmodiferade implantat (Studie IV-VI) och porösa implantat (Studie VII-VIII) studerats med olika mikroskopitekniker och komplementär spektroskopi. Osteocytlakunens form linjerar sig utefter riktningen på benmineralen i underliggande benvävnaden. Den lokala miljön i lakunen efter cellapoptos skiljer sig från kringliggande benvävnad vilket möjliggör utfällning av en annan kalciumfosfatfas, magnesium whitlockite, vilken är stabilare än apatit vid lägre pH. En återkoppling av kanalerna (canaliculi) mellan osteocytlakunerna i gammalt (benfragment från borrning) och osteocytlakunerna i det nybildade benets yta antyder en regenerativ kapacitet hos osteocyterna. Laserablering av implantatytan ökar den mekaniska förankringen efter inläkning. Vidare så återfinns osteocyter nära implantatytan med canaliculi som är i direkt kontakt med den mikro- och nanostrukturerade implantatytan. De mineraliserade kollagenfibrerna är ordnade på liknande vis vid ben-implantatytan som vid ben-osteocytlakunen. Fler osteocyter återfinns kring den skrovliga nativa additivt tillverkade implantatytan jämfört med den svarvade ytstrukturen. Vidare så återfinns osteocyter i direkt kontakt med koboltkrombaserade implantat, en legering som generellt anses ha sämre inläkningsförmåga jämfört med titanbaserade implantatmaterial. Sammanfattningsvis så visar dessa studier att osteocyterna ger viktig information om benets struktur och kvalitet och är således viktiga strukturella markörer för att förstå osseointegrationen. Utvärdering av osteocytnätverket är en viktig parameter vid testning av framtidens implantat avsedda för permanent förankring och belastning.

LIST OF PAPERS

This thesis is based on the following studies, referred to in the text by their Roman numerals.

I. Shah FA, Zanghellini E, Matic A, Thomsen P, Palmquist A. The Orientation of Nanoscale Apatite Platelets in Relation to Osteoblastic–Osteocyte Lacunae on Trabecular Bone Surface. *Calcif Tissue Int*. 2016;98:193-205.

II. Shah FA, Lee BEJ, Tedesco J, Wexell CL, Persson C, Thomsen P, Grandfield K, Palmquist A. Micrometre-sized magnesium whitlockite crystals in micropetrosis of bisphosphonate-exposed human alveolar bone. *Submitted for publication*.

III. Shah FA, Palmquist A. Evidence that Osteocytes in Autogenous Bone Fragments can Repair Disrupted Canalicular Networks and Connect with Osteocytes in *de novo* Formed Bone on the Fragment Surface. *Calcif Tissue Int*. 2017;101:321-327.

IV. Shah FA[#], Johansson ML[#], Omar O, Simonsson H, Palmquist A, Thomsen P. Laser-Modified Surface Enhances Osseointegration and Biomechanical Anchorage of Commercially Pure Titanium Implants for Bone-Anchored Hearing Systems. *PLoS One*. 2016;11:e0157504.
[#]Contributed equally.

V. Shah FA, Nilson B, Brånemark R, Thomsen P, Palmquist A. The bone-implant interface – nanoscale analysis of clinically retrieved dental implants. *Nanomedicine*. 2014;10:1729-37.

VI. Shah FA, Wang X, Thomsen P, Grandfield K, Palmquist A. High-Resolution Visualization of the Osteocyte Lacuno-Canalicular Network Juxtaposed to the Surface of Nanotextured Titanium Implants in Human. *ACS Biomater Sci Eng*. 2015;1:305-313.

VII. Shah FA, Snis A, Matic A, Thomsen P, Palmquist A. 3D printed Ti6Al4V implant surface promotes bone maturation and retains a higher density of less aged osteocytes at the bone-implant interface. *Acta Biomater*. 2016;30:357-367.

VIII. Shah FA, Omar O, Suska F, Snis A, Matic A, Emanuelsson L, Norlindh B, Lausmaa J, Thomsen P, Palmquist A. Long-term osseointegration of 3D printed CoCr constructs with an interconnected open-pore architecture prepared by electron beam melting. *Acta Biomater*. 2016;36:296-309.

Additional publications not included in this thesis:

I. Palmquist A, Shah FA, Emanuelsson L, Omar O, Suska F. A technique for evaluating bone ingrowth into 3D printed, porous Ti6Al4V implants accurately using X-ray micro-computed tomography and histomorphometry. *Micron*. 2016;94:1-8.

II. Wang X, Shah FA, Palmquist A, Grandfield K. 3D characterization of human nano-osseointegration by on-axis electron tomography without the missing wedge. *ACS Biomater Sci Eng*. 2016;3:49-55.

III. Shah FA, Stenlund P, Martinelli A, Thomsen P, Palmquist A. Direct communication between osteocytes and acid-etched titanium implants with a sub-micron topography. *J Mater Sci Mater Med*. 2016;27:167.

IV. Shah FA, Trobos M, Thomsen P, Palmquist A. Commercially pure (cp-Ti) *versus* titanium alloy (Ti6Al4V) materials as bone anchored implants – Is one truly better than the other? *Mater Sci Eng C Mater Biol Appl*. 2016;62:960-966.

V. Shah FA, Johansson BR, Thomsen P, Palmquist A. Ultrastructural evaluation of shrinkage artefacts induced by fixatives and embedding resins on osteocyte processes and pericellular space dimensions. *J Biomed Mater Res A*. 2015;103:1565-1576.

VI. Shah FA, Grandfield K, Palmquist A. Laser surface modification and the tissue–implant interface. Laser Surface Modification of Biomaterials: Woodhead Publishing; 2016.

CONTENT

1 INTRODUCTION

1.1 Bone quality

What is meant by *bone quality*? Being a hierarchical material [1], the overall strength of bone is determined by the combination of material composition and the unique structural design [2]. Examples of other hierarchically structured biological materials include abalone nacre, glass sponges, and antler bone [3, 4]. Bone exhibits several levels of organisation with repetitive structural units at different length scales [5, 6]. The extracellular matrix is mainly comprised of type-I collagen as the organic matrix phase, and ion substituted, carbonated apatite as the inorganic reinforcing phase. As a structural template, collagen functions together with mineralisation inhibitors to control the nucleation of amorphous calcium phosphate [7], orientates subsequent crystal growth, and is responsible for the size and distribution of apatite crystals in bone [8]. Additional factors such as acidic phospholipids and proteolipids, and non-collageneous macromolecules including osteopontin, osteocalcin, osteonectin, and bone sialoprotein also act as promoters or inhibitors of mineralisation [9], depending on factors such as phosphorylation, hydration, concentration, and conformation.

Collagen mineralisation occurs both interfibrillar [10] and intrafibrillar [11]. More than 30% of the mineral is extrafibrillar, ≤ 42% is contained within the 40 nm wide *gap* zones, and ≤ 28% is contained within the 27 nm wide overlap zones in the 67 nm cross-striated pattern of collagen [12]. At smaller length scales, mineralised collagen fibrils, ~100 nm in diameter [1], are the basic building block of bone material. At intermediate and subsequently larger length scales, collagen fibrils and mineral platelets form highly anisotropic, 1–3 μm wide, fibre bundles or cylindrical rods [6], arranged into plywood-like sheets with angles of 45–80° between adjacent layers [13]. Beginning as an amorphous precursor to crystalline platelets [14], biomineralisation processes are under strict spatial control of organic biomolecules. The plate-like morphology of apatite indicates that crystal growth occurs at different rates in all three directions; the crystallographic *c*-axis grows rapidly along the collagen fibril direction and is the longest dimension, while growth of the *a*- and *b*- axes is restricted by collagen fibrils opposite to these faces [15]. For intrafibrillar crystallisation to occur, site-specific epitaxial nucleation and growth are not necessary since the amorphous mineral phase is shaped by collagen prior to crystallisation. As apatite crystallises in the form of platelets having a preferred orientation, the collagen primarily acts to constrain the growth of

the apatite along its fast growing (001) direction [16]. Tangentially surrounding and separating each adjacent pair of collagen fibrils are 200 nm long, 65 nm wide, ~5 nm thick apatite platelets, in stacks of four – as estimated from the average interfibril distance (~28 nm) [17-19] **(Figure 1)**. Interestingly, such an arrangement of collagen and apatite is not exclusive to bone, but is also seen in ivory dentine [20, 21]. Although mineral directionality is closely directed by the organic phase, what controls the spatial organisation of collagen fibrils remains unknown. It is postulated that osteoblasts play a role in orienting collagen fibrils through their basal processes [22].

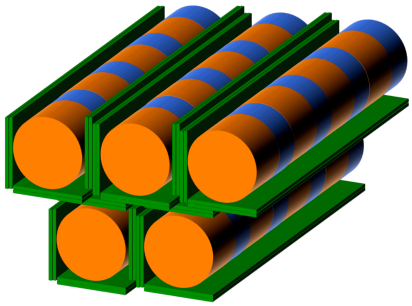

Figure 1. Simplified model of mineralised collagen fibrils: intrafibrillar mineral containing 40 nm long gap zone (orange), 27 nm long overlap zone (blue), and extrafibrillar mineral (green).

The relative mineral content and the degree of carbonate substitution are considered to be the strongest predictors of mechanical properties [23]. Increase in the degree of mineralisation [24], concurrently declining collagen content, and changes in inter- and intrafibrillar crosslinking [25] contribute towards reduced ductility and fracture toughness of bone with advancing tissue age. Substitution of CO_3^{2-} for OH^- and PO_4^{3-} changes the shape of the apatite crystal lattice [26], resulting in changes in the local strain environment, thus affecting the mechanical strength of a mineral crystal [27]. In synthetic carbonated apatites, increased mineral crystallinity results reduced carbonate content, i.e., decreased carbonate-to-phosphate ratio [28], but the mineral crystallinity in bone may remain unchanged despite an increase in carbonate-to-phosphate ratios [29]. While bone apatite does not contain a high concentration of OH^- groups [30], it is estimated that 40–50% of the OH^- groups are not substituted [31], and the amount of apatite hydroxylation is related to the degree of atomic ordering [32]. A range of analytical techniques can be used to investigate the hierarchical structure of bone [33], as well the ultrastructural organisation of collagen and apatite [34].

1.2 Bone formation and remodelling

Bone is formed by the production of organic matrix, by osteoblasts, and subsequent mineralisation of this organic matrix. Bone remodelling units are made up of osteoclasts and osteoblasts organised into a *cutting cone*, where resorption occurs at the apex, and new osteoid is deposited at the base. The total number of these remodelling units, and therefore the rates of resorption and formation of bone are relatively constant [35]. Bone mass is maintained across remodelling cycles through the coupling of cessation of resorption and initiation of formation, through bidirectional signalling between osteoclasts and osteoblasts [36]. Remodelling imbalance is a consequence of unbalanced relative activities of osteoblasts and osteoclasts. Increased osteoclast activation, whether due to hormonal control or diminished mechanical stimulation, leads to increased bone turnover, resulting in reduced bone mass. As a result of increased osteoclast activity there is disproportionate reduction in bone strength for the relative loss of bone mass. Combined with the formation of stress risers within the trabecular matrix, loss of bone strength and mass increases the risk of pathological (e.g., osteoporotic) fractures. Decreased osteoblastic activity contributes equally to this imbalance.

1.3 Osteocytes

Distributed throughout the mineralised extracellular matrix, osteocytes reside within confined spaces called *lacunae*, and are considered the master orchestrators of skeletal activity [37]. They play critical roles in bone formation and remodelling [38]. Osteocyte-driven control of bone formation is through the *SOST*/Sclerostin mechanism [39], while osteocyte-driven control of bone remodelling is through the signalling mechanism involving receptor activator of nuclear factor-κB ligand (RANKL), RANK, and osteoprotegerin (OPG) [40]. It is estimated that ~42 billion osteocytes reside within the average human skeleton, of which ~9 million osteocytes are replaced throughout the skeleton everyday [41]. From a polygonal shaped cell on the bone surface, i.e., as an osteoblast, the transformation towards a stellate phenotype is dramatic. The cell, once embedded in bone, especially cortical bone, has a polarity, particularly with respect to the direction of mineral formation [42]. Dendrite formation by embedding osteoid-osteocytes is initially polarised towards the bone surface, i.e., the mineralisation front. In the direction of blood vessels, dendrites begin to appear later once mineralisation begins to spread around the cell. Dendrite formation varies also between *static* and *dynamic* osteogenesis [43, 44]. Several theories have been proposed to explain the transformation of osteoblasts into osteocytes [45] **(Figure 2)**.

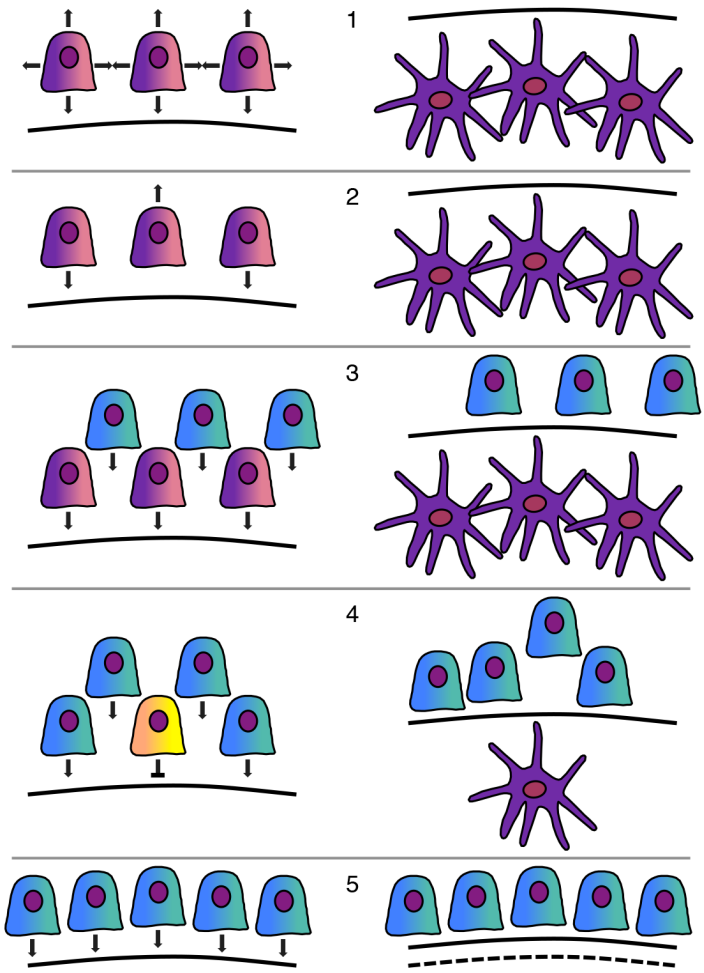

Figure 2. Theories of osteoblast-osteocyte transformation. 1. Bone is laid down in all directions by unpolarised osteoblasts, and the cells become trapped by their own secretions. 2. Individual osteoblasts are polarised and lay down bone in one direction only, but those within adjacent layers are polarised differently. Bone is deposited in all directions and osteoblasts become trapped. 3. Osteoblasts of each layer are polarised in the same direction and each successive generation buries the preceding one in bone matrix. 4. Within one layer, some osteoblasts slow down their rate of bone deposition, and become trapped by the secretions of their neighbouring cells. 5. Osteoblasts are highly polarised and function in a synchronised manner. The outcome is acellular bone as all cells move away from the bone formation front as bone matrix is deposited [inspired from [45]].

1.3.1 Sequence of entrapment and burial

Osteoblasts on the bone surface that are destined to undergo transformation into osteocytes slow down the production of extracellular matrix, relative to neighbouring osteoblasts [45]. Studies suggest that only one in ~67 osteoblasts is entrapped during the time interval necessary to complete the passages from the flattening of the preosteocyte to the closure of the lacuna [46], and eventual burial within the bone matrix [47] **(Figure 3)**. Inside a lamellar system, osteoblasts have limited freedom with regard to lateral sliding, and can only move in the direction perpendicular to the plane of bone apposition [22]. In the first and perhaps the only account of this nature, Jones *et al.* described an association between the shape and directionality of osteoblasts and the orientation of the underlying collagen fibres, and reported that up to 80% of the surface osteoblasts are oriented within 0° and 30° to the collagen fibre direction [48]. The cell membrane of the osteoblast shows corrugations and finger-like projections towards the bone surface, i.e., on the undersurface of the cell. Assuming temporal and spatial synchronisation of all the osteoblasts within the same layer, such morphological adaptations provide important insights into the regular polarisation and organisation of collagen fibrils into more compact bundles, in osteonal lamellae [22].

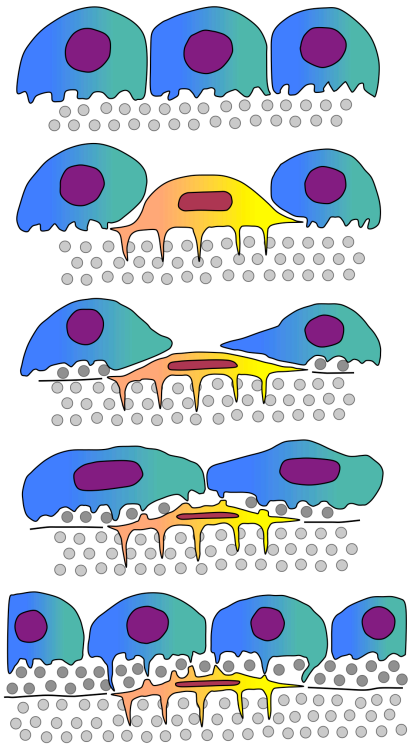

Figure 3. Sequence of changes in cell volume and cell shape during the osteoblast-osteocyte transformation. An osteoblast (yellow) slows down matrix production and becomes trapped within the matrix produced by neighbouring osteoblasts [inspired from [46]].

1.3.2 Osteocytes as mechanotransducers

Osteocytes, through their cellular processes [49-51] are highly mechanosensitive and alter the production of a multitude of signalling molecules triggered with a mechanical stimulus, enabling them to locally modulate osteoblast and osteoclast activity, *in vitro* [52] **(Figure 4)**.

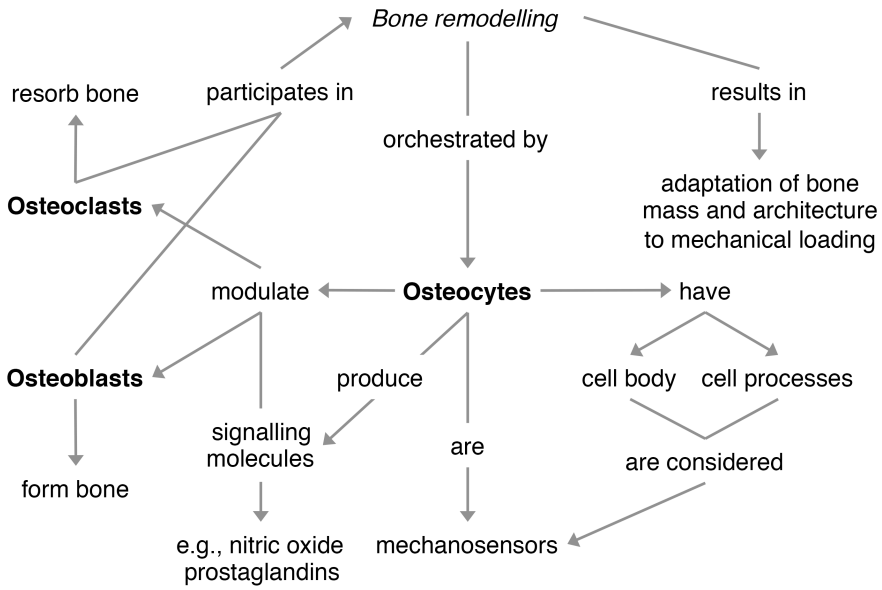

Figure 4. An overview of the central role that osteocytes play in bone remodelling [inspired from [53]].

1.3.3 Osteocyte apoptosis and micropetrosis

A condition in which osteocyte canaliculi, and the lacunae to a lesser extent, become occluded with mineralised tissue was termed *micropetrosis* by H. M. Frost [54], Fragments of apoptotic osteocytes within the lacunar space are replaced by mineral nodules [55, 56], which in osteoporotic human bone are poorly crystalline, magnesium-incorporated hydroxyapatite [57]. These mineral nodules may coalesce [58], thereby giving rise to hypermineralised lacunae that increase the fragility of ageing bone [59]. The osteocyte density has been shown to decline in association with accumulation of microdamage, with advancing age [60]. Osteocyte survival is a significant determinant of extracellular matrix volume [61], and a strong association exists between decreased osteocyte

density and increased porosity [62]. Moreover, osteocyte lacunar porosity can be used to predict bone matrix stiffness [63].

1.3.4 The enigma of anosteocytic bone

Interestingly, not all bone contains visible osteocytes. This is particularly true for certain types of fish, e.g., billfish [64-66]. But despite the lack of osteocytes and a rather *featureless* appearance, there is evidence for bone remodelling, for instance the presence of overlapping secondary osteons indicative of intensive tissue repair. But without the presence of strain-sensing osteocytes, these observations challenge one of the most fundamental concepts in bone biology – osteocyte-driven remodelling.

1.4 The lacuno-canalicular system

The lacuno-canalicular network (LCN), however, closely represents the pattern of bone formation [67] and correlates with bone material quality [68]. In human osteonal bone, the average length of the canalicular network is estimated at 0.074 ± 0.015 $\mu m/\mu m^3$ [69]. The formation of disordered, woven bone precedes the formation of organised lamellar tissue [70]. The presence of a substrate layer, on which surface osteoblasts can assemble and align, assists in the formation of an ordered tissue whereby the collagen fibrils are arranged in parallel over distances beyond the range of a single cell [68]. The secretory territory of rat osteoblasts on the parietal bone is approximately 154 μm^2 per osteoblast [71]. The spatial organisation of the extracellular matrix over a length scale corresponding to the size of many matrix-producing cells requires a coordinated action of the bone forming cells, further emphasising that initial spatial arrangement of these cells is a critical determinant [68].

In osteonal bone, a highly oriented network of osteocytes is aligned in nearly concentric layers connected by a multitude of canaliculi [72]. Between these cell layers are highly organised bone lamellae with near parallel collagen fibre orientation. In regions of older bone, canaliculi exhibit a disrupted appearance attributable to the remodelling process, and deposition of a cement line delineating the interface between the old and newly formed osteons. Canalicular density is greatly reduced in the vicinity of the cement line, confirming the notion that the surrounding old bone serves merely as a substrate for new bone deposition but does not necessarily guide it through signalling molecules [68]. Primarily formed, disordered woven bone lacks a predominant mutual alignment between osteocytes, and the canaliculi are directed mainly radially from the lacuna towards the neighbouring cells. As a result of fewer canaliculi, the connectivity between osteocytes is reduced in

comparison to organised lamellar bone. There is also a lack of long-range order of collagen fibrils, as they are arranged concentrically around the osteocytes and are thus perpendicular to the radial canaliculi alignment. This organisation of the collagen matrix can be defined as a microlamellar arrangement. The osteocytes in secondarily formed lamellar bone are mainly aligned in layers along bone lamellae, which are connected by canaliculi running perpendicularly through those layers. This difference in organisation suggests that a single osteoblast will only organise the tissue within a certain radius of action that is on the same order of magnitude as the spacing between osteocytes in microlamellar bone, ~20–30 μm [73]. However, osteoblasts are supported by a substrate, such as a layer of poorly organised bone, or a cement line, the surface osteoblasts are able to coordinate their activity such as to synthesise a layer of parallel ordered collagen over distances considerably larger than one cell [74].

1.5 Osseointegration

What is osseointegration, what osseointegration isn't, and what materials do not osseointegrate? In classical terms "*re- and new-formed bone tissues enclose the implant with perfect congruency to the implant form and surface irregularities thus establishing a true osseointegration of the implant without any interpositioned connective tissue*" [75]. Bone is considered a living tissue, but does bone ever stop being alive? What characterises living bone? Is there a component within bone, the presence or absence of which, distinguishes vital from non-vital tissue? It isn't the mineral phase. It also isn't the collagen which retains its integrity in mummified tissue even after 5300 years [76], and may be identified in poorly preserved Cretaceous period dinosaur bone [77].

The presently accepted definition of osseointegration is "*a direct – on light microscopic level – contact between living bone and implant*" [78]. More recently, the build-up of osseointegration has been described as an immune mediated foreign body reaction balance [79]. Is it enough to identify collagen-containing mineralised tissue abutting the surface of an implantable material, and consider it a sign of success, i.e., successful integration of an implanted alien material within bone – osseointegration? Indeed, as a living tissue, bone must respond in a variety of ways to the behaviour and characteristics of the implanted material. Furthermore, once osseointegration is achieved, is there a component within bone that is able to sense its now altered surroundings, and respond to the presence of an osseointegrated implant? That component is the osteocyte.

Within the healing defect, it is essential to distinguish between bone that forms from the implant surface, i.e., in response to the surface physico-chemical properties of the implant surface, referred to as *contact osteogenesis* [80], and bone that forms to fill the available space. Several processes contribute to the latter. For instance, bone that forms on the bony margin of the surgical defect, referred to as *distance osteogenesis* [80], and *de novo* formed woven bone. Often enough, originating from surgical drilling, autogenous bone fragments can be identified in the early stages of healing, which are able to support bone formation directly on their surface [81, 82].

1.5.1 Can osseointegration be controlled?

An extensive body of published literature suggests that the biological response can be improved by varying physico-chemical properties of the surface and the bulk of implantable devices. However, this perception of an improved biological response (of bone) is mainly derived from the amount of mineralised bone occupying the surgically created defect after a predetermined healing period. For metals and alloys of clinical relevance, e.g., titanium, an association can be drawn between a favourable biological response and the spontaneously formed, passivating oxide layer, the physicochemical characteristics of which are important for biomineralisation [83]. Ca^{2+} and PO_4^{3-} ions are adsorbed more readily on (001) and (100) faces than on the (110) face [84]. Therefore, apatite precipitation proceeds fastest on the (001) face of rutile where the fast growing crystallographic directions apatite are oriented along the substrate plane and the (001) direction points outwards from the surface [85]. Evidence also suggests that for a given metal, and within certain limits, roughened surfaces perform better than smoother ones, i.e., the bone response is directly influenced by the implant surface topography [86]. In contrast, there is little evidence in support of changing the bulk composition, e.g., from commercially pure titanium (cp-Ti) to Ti6Al4V, to have a detectable effect on the biological response [87, 88]. Evidence suggests that even *bioinert* metals such as gold support bone formation to a certain extent [89]. The question then is, with the exception of metals having well-documented adverse reactions, e.g., nickel or copper, do most metals and alloys osseointegrate?

At this point, it must be stated that inferences about *in vivo* osseointegration cannot be made from *in vitro* experiments. Although viability, proliferation, differentiation, extracellular matrix production etc. of relevant types of cells cultured on implant surfaces can be tested, there are countless limitations and caveats in the interpretation and translation of such information. Clinically, the success of an implanted device intended for long-term, load-bearing

applications is determined by anchorage and retention. The retention of an implanted device is determined by the proportion of the implant surface interfacing mineralised bone (i.e., bone-implant contact) without intervening soft tissue in addition to the extent of bone filling (i.e., bone area, or bone volume). Indeed, other parameters such as *bone quality* have an important role to play in establishing whether the formed bone is healthy and mechanically competent. Bone quality encompasses the microstructure as well as the composition of the extracellular matrix.

1.6 The bone-implant interface

In the context of this thesis, the term '*implant*' is restricted to metal or alloy devices intended for permanent anchorage in bone. The term '*interface*', however, takes on a considerably broader meaning. Etymologically, interface (noun) is "*a surface forming a common boundary between two portions of matter or space, for example between two immiscible liquids*" [90]. However, interface (verb) also means "*(to) interact with*" [90]. The bone-implant interface must therefore be understood as a wide zone in which many kinds of complex physical and chemical interactions take place between the surface of an inanimate implant and the surrounding physiological system.

In contrast to degradable biomaterials, such as ceramics and polymer composites, where the boundary between the material surface and the surrounding tissue migrates over time [91], the boundary between non-degradable metals or alloys and the surrounding tissue remains static. It is therefore possible to make inferences, morphologically, about the direction of bone formation with respect to the implant surface. Furthermore, changes in the extracellular matrix composition and structure with respect to healing time and distance from the implant surface can be readily explored. Localised variations in tissue composition, therefore, can provide extensive information about the dynamic processes of extracellular matrix formation and mineralisation, and bone turnover at the bone-implant interface.

Historically, the ultrastructural arrangement of the bone-implant interface has been subject to much debate since a large number of variables, including the *in vivo* model and species-specific characteristics, healing time point(s), physico-chemical properties of the implant surface, implant geometry, sample preparation route(s) and associated artefacts, analytical technique(s) and their limitations, and the use of systemically compromised animals to study bone healing in conditions such as osteoporosis, diabetes etc. In the early years, bone healing around metal implants was investigated mainly by histology and transmission electron microscopy (TEM). While histology

required extensive sawing and grinding, the *Sage-Schliff* technique, as described by Donath and Breuner [92] in their seminal work on studying mineralised tissues without the need for decalcification, preparation of ultrathin specimens for transmission electron microscopy remained a formidable challenge. It is difficult to obtain reproducible, electron transparent sections of mineralised bone abutting a metal implant using ultramicrotomy – the state-of-the-art technology available at the time for routine work. Some of the challenges were overcome through creative sample processing strategies and altering the implant design. For instance, instead of bulk metal, polycarbonate plugs onto which a thin layer of titanium could be deposited were utilised by Albrektsson *et al*. [93]. With this approach, Linder *et al*. [94] identified collagen fibrils as close as 20 nm of the titanium surface while osteocytes were found to approach the implant surface through cytoplasmic extensions. The so-called *fracture technique* was developed by Thomsen and Ericson [95], whereby the metal implant was separated from the resin embedded bone under a dissecting microscope. This, however, necessitated decalcification in 10% ethylenediaminetetraacetic acid (EDTA; $C_{10}H_{16}N_2O_8$) for up to three weeks. Although this method precluded investigation of the mineral component of the extracellular matrix, the organic and cellular components could still be visualised.

The idea of separating the metal implant from the resin embedded bone was further explored in a series of investigations by Steflik *et al*. [96-98] to evaluate, relatively thick, undecalcified sections by high-voltage transmission electron microscopy. These experiments revealed a mineralisation pattern of the implant surrounding bone that was similar to those events occurring naturally within the host bone. Osteocytes within lacunae were routinely found close to the implant interface and their morphology was similar irrespective of the distance from the implant surface. They reported an electron dense deposit at the interface, approximately 20–50 nm thick, and densely mineralised collagen fibrils running parallel to the implant surface. This dense mineralised tissue was separated from the interface by a mineralised but finely fibrillar matrix, approximately 200 nm thick. They also observed osteocyte processes within canaliculi extending directly to the implant surface. They proposed that the bone-implant interface zone is primarily fibrillar, both mineralised and unmineralised, and that unmineralised extracellular matrix initially is laid down directly at the implant surface, and this matrix is subsequently mineralised. Sennerby *et al*. [99] also reported canaliculi extending from osteocytes close to the implant surface.

Yet another description of the *in vivo* bone-implant interface was that of an approximately 500 nm thick, *collagen-deficient* cement line matrix, proposed

by Davies [100], based on osteogenic cell cultures in the absence of ascorbic acid, whereby collagen production is prevented. This cement line matrix appears globular and interdigitates with the implant surface. Interestingly, *in vivo*, such a cement line matrix has only been demonstrated after mechanical separation of the bone from the implant, and visualising thin remnants of bone that remained attached to the implant surface after the samples with sodium hypochlorite (NaOCl; 3% solution) [101, 102], a reagent used frequently to deproteinise bone [103, 104]. In normal bone, however, the precise composition of cement lines associated with secondary osteons, whether poorly mineralised [105] or collagen deficient [106], is heavily disputed. Using immunocytochemical techniques, the non-collagenous component of the organic matrix was explored by Nanci and co-workers [107, 108] who reported accumulation of osteopontin and bone sialoprotein at the bone-implant interface. Using a modified fracture technique in combination with immunocytochemical techniques, Ayukawa *et al.* [109] identified osteocalcin, in addition to osteopontin, at the bone-implant interface. Although these strategies were instrumental in generating fundamental information regarding the nature of the bone-implant interface, they had considerable limitations. For instance, the presence of type-I collagen had been interpreted from the periodic cross-striated pattern of alternating gap and overlap zones, as seen in normal bone. Importantly, electron dense areas were simply assumed to be *hydroxyapatite*, without specific identification of the mineral phase. TEM was only used for imaging and no associated analytical techniques were used. The use of focused ion beam scanning electron microscopy (FIB-SEM) revolutionised the preparation of electron transparent samples of the bone-metal interface for TEM. FIB-SEM made it possible to obtain, in a site-specific manner, intact specimens without the need for separating the metal from bone or decalcification of mineralised bone. The presence of hydroxyapatite was demonstrated adjacent to an anodically oxidised cp-Ti dental implant [110]. Later, the presence of hydroxyapatite was also demonstrated adjacent to a few nanometre-thick amorphous titanium oxide layer on a machined, cp-Ti orthopaedic implant [111].

1.7 Enhancing osseointegration

Osteoconductivity of titanium implants can be improved by increasing the surface roughness, and therefore also the surface area [86, 112]. The most frequently used methods have been titanium plasma-spraying, grit blasting, acid etching, and anodic oxidation [113]. For example, anodically oxidised cp-Ti implants enhance the biological response through regulation of mechanisms involving RANK, RANKL, and OPG [114].

Increase in surface area by introduction of nanoscale topography greatly increases the surface energy, which consequently increases the wettability of the surface. Higher wettability increases the affinity of the surface for blood and adsorption of fibrin and other biomolecules. Nanotextured surfaces therefore favour cellular attachment and tissue healing, and promote processes occurring immediately after implantation [115, 116]. TiO_2 nanotubes, ~100 nm outer diameter and ~10 nm wall thickness, produced by anodic oxidation have been shown to greatly improve *in vivo* mechanical retention [117]. By altering the composition of the electrolyte solution, and other parameters such as voltage and current density, the physico-chemical properties of anodically oxidised surfaces [118], and the diameter and the spacing between nanotubes [119] can be modulated. The precise dimensions of nanoscale features on the implant surface, e.g., generated by oxidative nanopatterning, can have a profound effect on cellular response [120-122].

1.7.1 Contamination-free hierarchical structuring

For modification of metal and alloy surfaces, the laser is a versatile tool [123], and offers several key advantages over traditional methods such as grit-blasting, acid-etching, and anodic oxidation. Of these, the foremost is the possibility to achieve site-specific surface alteration. For example, hierarchical textures comprised of pits, grooves, and ablation tracks can be created at intentionally selected locations. This is challenging to achieve with traditional methods where the surface modification is applied homogenously to the entire exposed surface. At relatively low pulse energies, high laser output power can be achieved by high pulse repetition rates or by short pulse durations. Picosecond (10^{-12} s) and femtosecond (10^{-15} s) [124-126] lasers thus allow extremely high precision machining of metals, with low thermal load, and no chemical reaction products. Importantly, in contrast to the more conventional techniques, contaminants are not introduced onto the surface during the laser machining process [127, 128]. For clinically relevant metals such as titanium, localised increase in temperature and reaction with ambient oxygen results in the development of a thickened surface oxide layer, which influences the osteoconductive behaviour and facilitates tissue bonding [129]. Melting and resolidification upon cooling of metal at the surface greatly enlarge the available surface area with obvious benefits for biomechanical anchorage of implantable devices. Frequently used lasers include the Neodymium-doped yttrium aluminium garnet (Nd:YAG), Copper-vapour laser, Nd:Glass (silicate or phosphate glasses), and the Excimer laser.

1.7.2 3D printing of open-pore geometries

Additive manufacturing has the potential to overcome many of the challenges faced in traditional machining of metals [130, 131]. Structures are built up by sequentially melting successive thin layers of powder. Material is added, not removed, and complex innovative designs can be produced in an intentional, controlled, predetermined manner. Medical implants with integrated open-pore architectures can be readily produced from a computer-aided design (CAD) file, enabling either mass production of well-defined implants or customised implants based on patient-specific diagnostic imaging [132, 133]. Electron beam melting (EBM) is one such additive manufacturing technique used for load bearing metal implants whereby the overall stiffness of constructs of clinically relevant metals and alloys can be tailored [134].

For orthopaedic applications, metal implants having an interconnected open-pore structure are of particular interest due to their potential ability to facilitate tissue ingrowth, and present the possibility for reducing the stiffness mismatch between the load-bearing metal implant and bone, thus eliminating stress-shielding effects [135]. Due to their high stiffness, metallic devices take most of the load, producing stress shielding in the adjacent bone. Reduced mechanical stimulation may induce resorption of surrounding bone, leading to implant loosening and failure of osseointegration [136, 137].

With the use of EBM, the elastic modulus of porous Ti6Al4V can be tailored to be similar to that of bone, thus minimising the stress shielding effect [138]. The native EBM surface allows bone ingrowth into the surface irregularities, with bone-implant contact levels at par with machined surfaces prepared by wrought and EBM techniques [139]. Moreover, implants with an interconnected open-pore structure support bone formation not only around the implant but also within the porous network, with high levels of bone-implant contact and bone volume [140]. As the starting powders for EBM are prepared by atomisation, the powder particles used in the fabrication process and therefore the surfaces of EBM manufactured constructs do not exhibit a high degree of sub-micron scale roughness.

In addition to Ti6Al4V, CoCr alloys are also used extensively in orthopaedic reconstructive surgery for their high strength and wear properties [141-143]. The clinical results of uncemented, CoCr femoral stems, having a sintered porous surface appear promising [144], allowing bone ingrowth into the intricate porous coated surface [145]. Periprosthetic bone loss around femoral stems is a matter of concern, even with Ti6Al4V alloys, which otherwise have an outstanding clinical record. Postoperatively, while limited weight-bearing and aseptic

loosening are implicated as factors contributing to bone loss [146], it is believed that the high stiffness of CoCr is the primary cause of stress shielding and bone resorption [147]. The extent of stress shielding experienced by bone around a bone-anchored device depends on the interfacial bonding characteristics, e.g., whether the bone-anchored device is cemented or uncemented, the presence of a surface coating, and the possibility for bone ingrowth [137]. Stress shielding also dependent on the structural stiffness, which is principally related to the bulk and the elastic modulus of the material [137]. Indeed, the overall stiffness of a metal implant and the stress shielding in bone may be reduced by design modifications.

CoCr alloys are often considered inferior to titanium (typically Ti6Al4V) alloys in terms of osseointegration and biomechanical fixation [148, 149]. However, to make use of the superior mechanical and tribological properties of CoCr, attempts have been made to improve the biological response to CoCr implants the application of various coatings [150, 151]. Interestingly, no differences are observed between uncoated, solid Ti6Al4V and CoCr implants on the histological [152] and the ultrastructural [153] levels. Furthermore, recent findings suggest that EBM manufactured, solid, CoCr implants osseointegrate without adverse tissue reactions [154]. Nevertheless, bone ingrowth into porous CoCr constructs has not been evaluated, and little is known about the precise biological and tissue response to such materials.

1.8 Osseointegration in terms of bone quality

Does a strong, early osteogenic response to certain design features of an implant lead to mechanically and functionally competent tissue, with long-term alterations in bone quality? Implant surfaces believed to elicit a stronger osteogenic effect tend to do so, mainly, during early healing. Quantitative differences in the amount of bone formed as a result of the osteogenic potential attributed to an implant surface are often lost at longer follow up times. Injected fluorescent labels can be used to study bone formation kinetics [155, 156], but problems also arise with their use since these molecules bind to mineralised surfaces and alter certain characteristics of the mineral phase, including mean particle thickness and degree of alignment [157]. The following work addresses some of these questions, and investigates osseointegration in terms of bone quality, with particular emphasis on identifying compositional and ultrastructural patterns in the interfacial tissue at intermediate or late healing periods.

2 AIM

This thesis aims to establish novel correlative strategies, e.g., extracellular matrix composition and morphological changes in the osteocyte lacuno-canalicular (Ot.LCN) system, to characterise bone healing around metal and alloy implants, at intermediate and/or long healing periods.

2.1 Specific aims

The specific aims of the papers included in this thesis were the following:

–To determine the ultrastructural relationship between the shape of the osteoblastic-osteocyte lacunae (Ot.Lc) and the orientation and the directional coherency of mineral platelets at the Ot.Lc floor [Paper I].

–To investigate post-apoptotic mineralisation of the osteocyte lacuna in human alveolar bone, with and without bisphosphonate exposure [Paper II].

–To evaluate if osteocytes in autogenous bone fragments, generated during implant site preparation, can restore disrupted canalicular networks and connect with osteocytes in *de novo* formed bone on the surface of such fragments [Paper III].

–To investigate the biomechanical anchorage and osseointegration of laser-modified, cp-Ti implants having a hierarchically structured surface in a rabbit model after eight weeks *in vivo* [Paper IV].

–To study osseointegration of functionally loaded, laser-modified, cp-Ti implants having a hierarchically structured surface [Paper V], and the ultrastructure of the osteocyte-implant interface [Paper VI] in human after four years *in vivo*.

–To investigate osseointegration of 3D printed, macroporous and solid Ti6Al4V implants in a sheep model after six months *in vivo* [Paper VII].

–To investigate osseointegration of 3D printed, macroporous CoCr and Ti6Al4V implants in a sheep model after six months *in vivo* [Paper VIII].

3 MATERIALS AND METHODS

In the following work, several *in vivo* models, anatomical locations, implant materials and their geometry, and specific design features were included **(Table 1)**. Experiments involving human alveolar bone biopsies [Paper II] were approved by the Regional Ethical Review Board, Göteborg. Experiments involving rats [Paper III] and rabbits [Paper IV] were approved by the local Animal Ethics Committee at the University of Gothenburg, Göteborg. All procedures performed in studies involving animals or humans were in accordance with the ethical standards of the institution at which the studies were conducted.

3.1 Implant fabrication

3.1.1 Selective laser ablation

Site-specific surface modification was achieved by ablation with a Q-switched Nd:YAG laser (Rofin-Sinar Technologies Inc., Plymouth, USA). The technique allows generation of a pulsed output beam, with extremely high peak power, considerably higher than would be produced by the same laser operated in a constant output (continuous wave) mode. A pulsed 1064 nm wavelength laser focused to spot sizes of 100–125 μm was operated in ambient air, on rotating implants to achieve a hierarchical structure of 1–10 μm features with a superimposed nanotexture confined to the implant thread valley, reaching no greater than 30% of the thread height on each flank [Papers IV–VI].

3.1.2 Electron beam melting

Two types of Ti6Al4V implants, solid and porous, were manufactured in an Arcam EBM S12 system. The porous implants retained the EBM surface. To obtain the solid implants, cylindrical rods produced during the same build cycle were machined to remove the EBM surface [Paper VII]. Porous, Ti6Al4V and CoCr implants were manufactured in an Arcam EBM A1 system [Paper VIII]. All EBM produced implants were 7 mm in length and 5.2 mm in diameter. Plasma-atomised Ti6Al4V and gas-atomised CoCr powders, having particle sizes < 100 μm, were used. The average build temperatures were 680°C for Ti6Al4V and 780°C for CoCr. All implants were blasted with the same powder as they were built of and a shallow notch was machined in the top surface to facilitate implant placement.

Table 1. Summary of in vivo models, anatomical locations, implant materials and their geometry, and specific design features included in this thesis.

	Bone		*Implant*	
Paper	**Species**	**Location**	**Material and geometry**	**Design features**
I [158]	Sheep	Tibia, femur		
II	Human	Alveolar bone (maxilla, mandible)		
III [159]	Sprague Dawley rat	Tibia	Cp-Ti. 2 mm diameter; 2.3 mm length. Screw-shaped	With and without commonly applied surface modifications
IV [160]	New Zealand white rabbit	Tibia	Cp-Ti. 3.75 mm diameter; 5 mm length. Screw-shaped	Nd:YAG laser ablation. Machined (Ctrl)
V [161]	Human	Alveolar bone (maxilla)	Cp-Ti. 3.5 mm diameter; 13 mm length. Screw-shaped	Nd:YAG laser ablation
VI [162]	Human	Alveolar bone (maxilla)	Cp-Ti. 3.5 mm diameter; 13 mm length. Screw-shaped	Nd:YAG laser ablation
VII [163]	Sheep	Distal femur	Ti6Al4V. 5.2 mm diameter; 7 mm height. Macroporous; cylindrical rods	EBM; EBM+Machined (Ctrl)
VIII [164]	Sheep	Distal femur	Ti6Al4V; CoCr. 5.2 mm diameter; 7 mm height. Macroporous	EBM

3.2 Analytical techniques

3.2.1 Scanning electron microscopy

In a scanning electron microscope (SEM), interaction between the incident electrons and atoms in the sample generates various signals that contain information about the topography and composition of the sample surface. High vacuum conditions in a conventional SEM require samples to be clean, dry, and electrically conductive. Non-conductive samples must be coated with a conductive film to avoid static charge build-up.

Secondary electron imaging

Secondary electrons (SE) are low-energy (< 50 eV) electrons typically ejected from the K shell of the atoms in the sample, as a result of inelastic scattering interactions with the incident electrons. SEs originate from within a few nanometres from the sample surface due to their low-energy, and are collected by the electrically biased (300–400 V) Everhart-Thornley detector, positioned off axis. An in-lens detector positioned in a rotationally symmetric arrangement inside the electron column can also collect SEs. At low accelerating voltages, images can be generated with high contrast based on the work function on the sample. Therefore, in addition to surface topography, information about the composition can also be obtained at high lateral resolution. In this work, an Everhart-Thornley detector has been used for imaging deproteinised bone and the osteocyte lacuno-canalicular network (Ot.LCN) after resin cast etching, while an in-lens detector has been used for imaging implant surfaces.

Backscattered electron imaging

Backscattered electrons (BSE) are high-energy electrons that are deflected by very high angles out of the specimen interaction volume by elastic scattering interactions with atoms in the sample. The BSE *Z*- (atomic number) contrast can be used to detect contrast between regions on the sample surface having different average atomic numbers, since heavier elements (high *Z*-) backscatter electrons more efficiently than lighter elements (low *Z*-) and thus appear brighter in the image. BSE detectors are positioned above the sample in a ring shaped arrangement, concentric with the electron beam. In this work, the BSE mode has been used to image polished surfaces of mineralised bone, where well-mineralised regions give high *Z*- contrast while unmineralised structures such as osteocyte lacunae exhibit low *Z*- contrast and can be easily identified and quantified.

Environmental scanning electron microscopy

Non-conductive samples can be imaged without modification from their natural state in an environmental scanning electron microscope (ESEM). Thus their original characteristics may be preserved. An imaging gas, typically water vapour, is introduced into the sample chamber. These gas molecules can scatter the electrons and degrade the electron beam. Therefore high vacuum is maintained throughout the electron column, by using multiple pressure limiting apertures to isolate the sample chamber from the electron column rather than using a single pressure limiting aperture (as in a conventional SEM). The sample chamber may, however, sustain high pressures. A highly energetic primary electron beam penetrates the water vapour with little apparent scatter. SEs released from the sample surface (as in a conventional SEM) encounter water vapour molecules. When hit by the SEs, the water vapour molecules produce SEs themselves, which in turn produce SEs from neighbouring water vapour molecules. The original SE signal from the sample is thus amplified, and collected at the electrically biased (600 V) gaseous secondary electron detector (GSED). BSEs pass through the gaseous volume and induce additional ionisation and generate amplification. In an ESEM, static charge build-up is neutralised by the strong positive bias on the GSED, driving the now positively charged water vapour molecules towards the sample surface. In this work, an ESEM has been used for BSE imaging of mineralised bone and determining osteocyte density, the average number of osteocytes per mineralised surface area (N.Ot/B.Ar).

Resin cast etching

The resin cast etching technique uses resin embedded bone or bone-implant blocks to expose and directly visualise the three-dimensional Ot.LCN **(Figure 5)**. This is achieved by preferential removal of mineralised tissue leaving resin-infiltrated osteocyte lacuno-canalicular and the vascular networks intact. The samples are initially wet polished using SiC paper from 400 grit (~35 μm particle size) to 4000 grit (~2.5 μm particle size). Regions of interest are identified by low vacuum BSE imaging in an ESEM. The resin embedded blocks are then immersed sequentially in 9% ortho-phosphoric acid and 5% sodium hypochlorite to remove the inorganic and organic components, respectively, leaving behind a resin filled cast of osteocytes, canaliculi, and blood vessels. The samples are sputter coated with a thin Au layer (~10 nm) for high vacuum SE imaging. Resin cast etching has been used to determine the osteocyte density, i.e., the average number of osteocytes per mineralised surface area (N.Ot/B.Ar) and the number of osteocyte canaliculi per osteocyte lacuna (N.Ot.Ca/Ot.Lc).

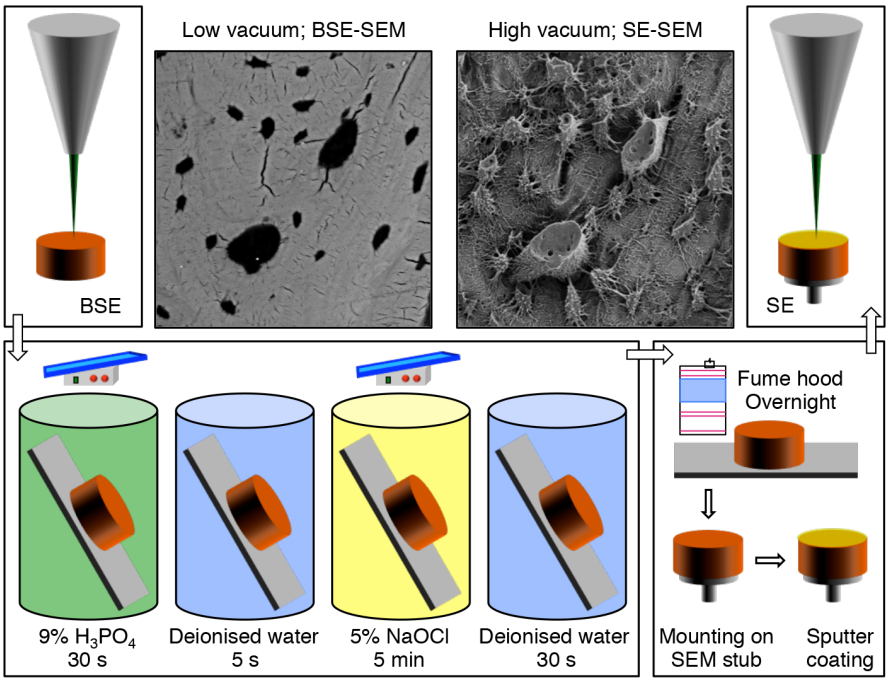

Figure 5. Resin cast etching technique for direct visualisation of the osteocyte lacuno-canalicular network.

3.2.2 Transmission electron microscopy

In a transmission electron microscope (TEM), an accelerated beam of electrons travels through an electron transparent (~100 nm thick) sample, resulting in a variety of interactions between the incident electrons and the atoms in the sample. In bright field TEM, the direct beam is collected, and therefore mass-thickness and diffraction contrast contribute to image formation. The information is a mixture of elastic and inelastic scattering. Scanning transmission electron microscopy (STEM) uses a fine, convergent electron beam that is rastered across the sample. At each step, the generated signal is simultaneously recorded by the detector(s) of choice. Such a convergent beam generates a highly localised signal from the sample, and is used for energy dispersive X-ray spectroscopy (EDX) and electron energy loss spectroscopy (EELS). High-angle annular dark field (HAADF-) STEM uses a ring-shaped detector that collects electrons scattered to very high angles and almost exclusively incoherent Rutherford scattering contributes to the image. *Z*- contrast is thus achieved. In comparison, annular dark field (ADF-) STEM also uses a ring-shaped detector, but of considerably smaller

diameter than the HAADF- detector. The electrons used for image formation are also scattered, but at smaller angles, and therefore the contrast mainly results from electrons diffracted in crystalline areas of the sample with some contribution from incoherent Rutherford scattering. This work mainly uses HAADF-STEM and bright field TEM for imaging the ultrastructural organisation of collagen and apatite in bone formed adjacent to implant surfaces. Electron transparent specimens were prepared using the in situ lift-out technique on a focused ion beam scanning electron microscope (FIB-SEM). In addition to an electron column, a FIB-SEM has an ion column positioned at 52° to the electron column. Using a finely focused beam of ions, e.g., gallium (Ga^+), imaging can be performed at low beam currents while high beam currents are used for site-specific milling.

Energy dispersive X-ray spectroscopy

Energy dispersive X-ray spectroscopy (EDX) uses the X-ray spectrum emitted by a sample when bombarded with a beam of sufficiently energetic electrons to obtain site-specific chemical analysis. A core hole is created when an atom in the sample is ionised by the primary electron beam. An electron from an outer shell transitions into the core hole, generating a characteristic X-ray with the corresponding energy. EDX can be performed in the SEM using bulk samples with minimal sample preparation, or in a TEM using electron transparent samples. In this work, EDX has been used to investigate the elemental composition of deproteinised bone, *de novo* formed bone on autogenous bone fragments, bone interfacing different implant surfaces, and hypermineralised osteocyte lacunae.

Electron energy loss spectroscopy

In electron energy loss spectroscopy (EELS), a thin sample is exposed to a beam of electrons of a known narrow range of kinetic energies. As they travel through the sample, some of the incident electrons undergo inelastic scattering, i.e., they lose energy and are deflected slightly from their original paths. The amount of energy lost can be measured using an electron spectrometer, to identify what caused the energy losses. Inner shell ionisations are useful for detecting the elemental constituents of a sample. In this work, EELS has been used to map the distribution of Ca at the bone-implant interface, and C, Ca, O in hypermineralised ostecyte lacunae.

Selected area electron diffraction

In a TEM, a thin specimen is subjected to a parallel beam of high-energy electrons. The atoms in the sample behave as a diffraction grating to the incident electrons, a fraction of which is scattered to specific angles, determined by the crystal structure of the sample. The resulting image, the

selected area diffraction (SAED) pattern, is a projection of the reciprocal lattice appearing as a series of spots or rings (or a combination of both), each corresponding to a satisfied diffraction condition of the sample's crystal structure. Single crystals exhibit discrete spot pattern while polycrystalline materials exhibit ring patterns. In this work, SAED has been used to determine the crystallographic orientation of bone apatite, and to identify and probe the degree of long-range calcium phosphate phases found in bone.

Electron tomography

Electron tomography (ET) and 3D reconstructions allow a comprehensive analysis of bone ultrastructure at interfaces [165-167]. An electron transparent sample is tilted over a predetermined angular range, e.g., ± 70°, HAADF-STEM images are collected at each tilt step, e.g., 1–2°. HAADF-STEM images suppress diffraction contrast, and the obtained information correlates with the elemental composition of the analysed volume.

3.2.3 Raman spectroscopy

Raman spectroscopy is based on inelastic scattering of photons, the Raman effect, by the molecules in a sample. Most photons are elastically scattered (Rayleigh scattering) whereby the emitted photon has the same wavelength (or energy) as the incident photon. On rare occasion (1×10^{-7} photons), the incident photon energy can excite vibrational modes of the molecules, resulting in the scattered photons having a frequency lower than that of the incident photons, and the difference in energy corresponds to the vibrational transition energy. This shift in energy of the inelastically scattered radiation provides chemical and structural information. In this work, Raman spectroscopy has been used to investigate the composition of bone, and the relative amounts of extracellular matrix components, e.g., phosphate groups (representing bone apatite), carbonate groups, amide groups (representing type-I collagen), as well as amino acids such as proline (Pro), hydroxyproline (Hyp), phenylalanine (Phe), tyrosine (Tyr) etc. The investigated Raman metrics included mineral crystallinity, taken as the reciprocal of the full-width at half-maximum (1/FWHM) of the ν_1 PO_4^{3-} peak, apatite-to-collagen ratio, also referred to as the mineral-to-matrix ratio (ν_2 PO_4^{3-}/Amide III; ν_1 PO_4^{3-}/Amide I), carbonate-to-phosphate ratio (ν_1 CO_3^{2-}/ν_1 PO_4^{3-}; ν_1 CO_3^{2-}/ν_2 PO_4^{3-}), carbonate-to-matrix ratio (ν_1 CO_3^{2-}/Amide I ratio), Amide I/Amide III ratio. The relative amounts of proline (Pro/ν_1 PO_4^{3-}), phenylalanine (Phe/ν_1 PO_4^{3-}), and tyrosine (Tyr/ν_1 PO_4^{3-}), phenylalanine-to-tyrosine (Phe/Tyr) ratio, and phenylalanine-to-carbonate (Phe/ν_1 CO_3^{2-}) ratios were also investigated. Additionally, Raman spectroscopy has been used to identify other calcium phosphate phases found within hypermineralised osteocyte lacunae.

3.2.4 Other analytical techniques

X-ray micro-computed tomography

X-ray micro-computed tomography (micro-CT) produces 3D images of the internal structure of a specimen, nondestructively, at micrometre level spatial resolution, and requires minimal sample preparation. The sample is continuously rotated, and a series of 2D X-ray projection images is acquired and mathematically reconstructed to generate a 3D map of X-ray absorption in the volume. In this work, micro-CT has been utilised for the assessment of implant geometry and bone formation in relation to metal implants.

Histology and histomorphometry

For histology and histomorphometry, this work has utilised ground sections stained with toluidine blue. It is a basic thiazine (C_4H_5NS) metachromatic dye that selectively stains acidic tissue components, particularly nucleic acids, sulphates, carboxylates, and phosphate radicals. The acidophilic nature of this stain can qualitatively indicate the extent of bone tissue maturation. Younger, (or recently formed) bone contains more acid phosphate groups (HPO_4^{2-}) to which the dye can bind, resulting in more intense staining than older bone. In bone-implant studies, histomorphometry is performed to determine the percentage bone-implant contact (BIC) and bone area (BA). Additionally, qualitative assessment of bone microstructure is performed to observe bone cells (osteoblasts, osteocytes, and osteoclasts), bone phenotype, bone marrow, inflammatory cells, fibrous tissue, and structures of non-biological origin such as wear debris from implant materials.

Nanoindentation

Indentation tests are used to measure mechanical properties, e.g., indentation hardness, H, and reduced elastic modulus, E_r, from a contact of known geometry [168, 169]. The indenter tip is made of diamond, formed into a three-sided symmetric shape such as the Berkovich tip. The Oliver–Pharr method [168] is used most frequently to determine H and E_r from the obtained load-deformation curves. H is calculated using the maximum load, P_{max}, and the contact area under load, A_c. E_r is related to elastic displacement in both the indenter and the specimen being investigated, and is dependent on the geometry of the probe, β and the stiffness at peak load, S. Typically, $\beta = 1.0$ for spherical indenters and $\beta = 1.034$ for a triangular Berkovich probe. S is the slope of the unloading curve at the maximum indentation depth, and is obtained by fitting the upper portion of the unloading curve to a simple power-law expression and measuring the slope at peak load. In this work, nanoindentation has been used to measure H and E_r of the extracellular matrix and hypermineralised osteocyte lacunae in human bone.

Biomechanical tests for implant stability and anchorage

Resonance frequency analysis (RFA) measures the stability of an implant as a function of the stiffness of the bone-implant interface. Using magnetic pulses, a sensor mounted on top of the implant is made to vibrate. The vibration frequency, or the Implant Stability Quotient (ISQ), ranges between ~1 and ~10 kHz (ISQ 1–100) and increases with increasing stability of an implant in bone, which is influenced by factors such as bone density, the degree of osseointegration, implant site preparation and implant design. Removal torque (RTQ) refers to the torsional force (in Ncm) necessary for unscrewing an implant and primarily measures interfacial shear properties.

Deproteinisation

The mineral phase of bone is visualised directly by rendering the bone anorganic. After chemical fixation, bone samples are soaked in 5% NaOCl at 4°C for up to 72 h, followed by gentle rinsing in deionised water and dehydration in a graded ethanol series (50–100%). The samples are allowed to air dry for 24 h and conductively coated for SEM. In this work, deproteinisation has been used to study the orientation of mineral structures seen at the floor of lacunae associated with partially embedded osteocytes.

Image analysis of mineral directionality

The directionality of structures within an elliptical region of interest (ROI), e.g., the floor of lacunae associated with partially embedded osteocytes seen using SEM after deproteinisation, was measured in ImageJ (*imagej.nih.gov/ij*). The ROI outline is defined by manual selection of ≥ 20 points, followed by applying a least squares fit ellipsoid to identify the long axis of the ROI. The ROI is minimally rotated so that the long axis lies in the horizontal plane. The mean orientation with respect to the horizontal plane and coherency (of alignment) of structures is obtained using the OrientationJ plugin [170]. Parameters are adjusted for particle size and pixel size considerations.

Auger electron spectroscopy

In Auger electron spectroscopy (AES), the sample is exposed to a beam of high-energy electrons capable of creating a core hole. The ionised atom relaxes rapidly as an electron from a higher energy level transitions to fill the initial core hole. The energy thus emitted is transferred to a second electron. A fraction of this energy is required to overcome the binding energy of this second electron, the remainder is retained as kinetic energy by this emitted *Auger* electron. The final state is an atom with two core holes. The initial ionisation is non-selective and the initial hole may be in various shells, therefore several possible Auger transitions exist for a given element. The kinetic energies of the emitted electrons are independent of the initial core

hole. Therefore each element in a sample gives rise to a characteristic spectrum of peaks at various kinetic energies. In this work, AES has been used here to determine the elemental composition of the implant surface.

X-ray photoelectron spectroscopy

X-ray photoelectron spectroscopy (XPS) is a highly surface-sensitive technique that can be used to determine the elemental composition, and the chemical and electronic states of the elements within a sample. XPS spectra are obtained by irradiating the sample surface with a beam of X-rays, and the kinetic energies and number of electrons that escape from the first few nanometres are measured. Each element produces a characteristic set of peaks at characteristic binding energy values corresponding to the electronic configurations of the atoms within the analysed volume. In this work, XPS has been used to determine the elemental composition of the implant surface.

White light interferometry

White light interferometry is a non-contact, optical technique for measuring the profile of a surface. A beam splitter separates a collimated beam of spectrally broad, visible light into two beams – one is reflected from the sample surface and the other is reflected from a reference mirror. Upon combining, the resultant fringe pattern is determined by the phase difference between them. Since white light has a short coherence length, the degree of fringe modulation is measured rather than the phase of the interference fringes. In this work, white light 3D interference microscopy has been used to measure the surface roughness of the implant surface.

3.3 Statistical analysis

For statistical analysis, parametric, One-way ANOVA and Student's *t*-test, and non-parametric tests, the Kruskal-Wallis test followed by the Mann-Whitney U test (for independent samples), and the Wilcoxon Signed Rank test (for pair-wise analysis) were used. One-way ANOVA was used for orientation and coherency of mineral platelets at the Ot.Lc floor [Paper I]. The Student's *t*-test was used for N.Ot.Ca/Ot.Lc [Paper VI]. The Kruskal-Wallis test followed by the Mann-Whitney U test were used for implant surface characterisation [Paper IV], Raman spectroscopy, EDX, and N.Ot/B.Ar [Papers VII–VIII], N.Ot.Ca/Ot.Lc [Paper VII], and H and E_r [Paper II]. The Wilcoxon Signed Rank test was used for biomechanical tests (RFA and RTQ) [Paper IV], histomorphometry [Papers IV and VIII], and Raman spectroscopy [Paper IV].All statistical analyses were performed using SPSS (IBM Corporation), and p values < 0.05 were considered statistically significant.

4 RESULTS

4.1 Paper I

This work investigates the relationship between the shape of lacunae associated with partially embedded osteocytes (osteoblastic-osteocytes) and alignment of the mineral phase of the underlying bone surface.

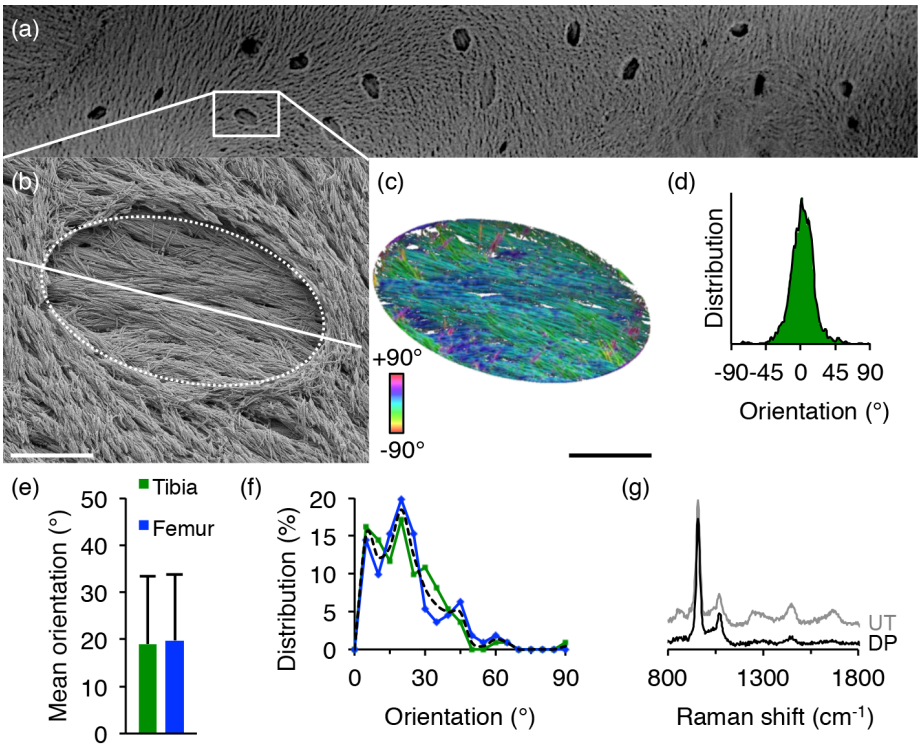

Figure 6. (a) Deproteinised trabecular bone surface. (b) An osteocyte lacuna (Ot.Lc) in high magnification. (c) Analysis of mineral orientation. (d) Distribution (in pixels) of structure tensors for the example in c. (e) Mean orientations of mineral platelets at the Ot.Lc floor in the tibia and the femur (n = 111). (f) A majority of Ot.Lc exhibit a mean orientation between 0° and 25°. Tibia = green; Femur = blue; Combined = black broken line. (g) Raman spectra of untreated (UT) and deproteinised (DP) bone. Scale bars in b and c = 5 µm.

Deproteinised trabecular bone surface consisted of bundles of mineral platelets arranged in a meshwork and lacunae associated with incompletely buried osteocytes. The Ot.Lc floor was composed of elongated 1–3 μm-wide mineralised bundles running nearly parallel to the Ot.Lc long axis **(Figure 6)**. Mineralised bundles external to the Ot.Lc were arranged in concentric patterns. These mineralised bundles were composed of numerous parallel platelets. Between these mineralised bundles were round holes left behind by osteocyte dendrites. External to the Ot.Lc, bundles from multiple successive layers were visible. Individual mineral platelets belonging to one bundle swiftly switched between adjacent bundles, thus forming an interconnecting mesh.

At the Ot.Lc floor, the mean orientation of mineral platelets relative to the Ot.Lc shape was 19° ± 14° in the tibia and 20° ± 14° in the femur. The coherency was 37 ± 7% in the tibia and 38 ± 9% in the femur. Histograms showing the distribution of structure tensors, generated as an average of all the Ot.Lc in each group, indicated that a major proportion of the structure tensors was oriented between 0° and 45° for both the tibia and the femur. A preferential orientation of the mineral platelets relative to the long axis of Ot.Lc was noted. A majority of the Ot.Lc, 69.37% of the Ot.Lc in the tibia and 74.77% in the femur, exhibited a mean orientation of mineral platelets between 0° and 25°. The largest fraction of Ot.Lc was oriented in the 15°–20° range, 17.12% in the tibia and 19.8% in the femur.

In an area of new bone formation, adjacent to a zone of osteoclast resorption tracks, the structure of the bone surface and the Ot.Lc floor were composed of repeating 1.5–2 μm long and 1 μm wide motifs. These were oriented similar to the fibre bundles observed in areas of more mature bone. In high resolution, these repeating structural units were comprised of 20–25 nm thick plate-like structures believed to be bone apatite separated approximately by the diameter of individual type-I collagen fibrils. These structural units at the Ot.Lc floor seemed to coalesce with advancing tissue maturity, thus giving the appearance of longer, continuous fibre-like structures that were better organised at the Ot.Lc floor than the surface external to the Ot.Lc where bundles of mineral platelets did not share a similar common orientation. In addition, numerous 390 ± 80 nm crystallites were observed sparsely scattered, but fused together with other mineral platelets over the surface.

Raman spectroscopy confirmed a significant increase in the mineral-to-matrix ratio of deproteinised bone compared to untreated bone, while mineral crystallinity and the carbonate-to-phosphate ratio remained unaffected.

4.2 Paper II

The work investigates the post-apoptotic mineralisation process within Ot.Lc in alveolar bone obtained from women who had received bisphosphonates (*BP*) and bone obtained from healthy, non-osteoporotic women (*Ctrl*).

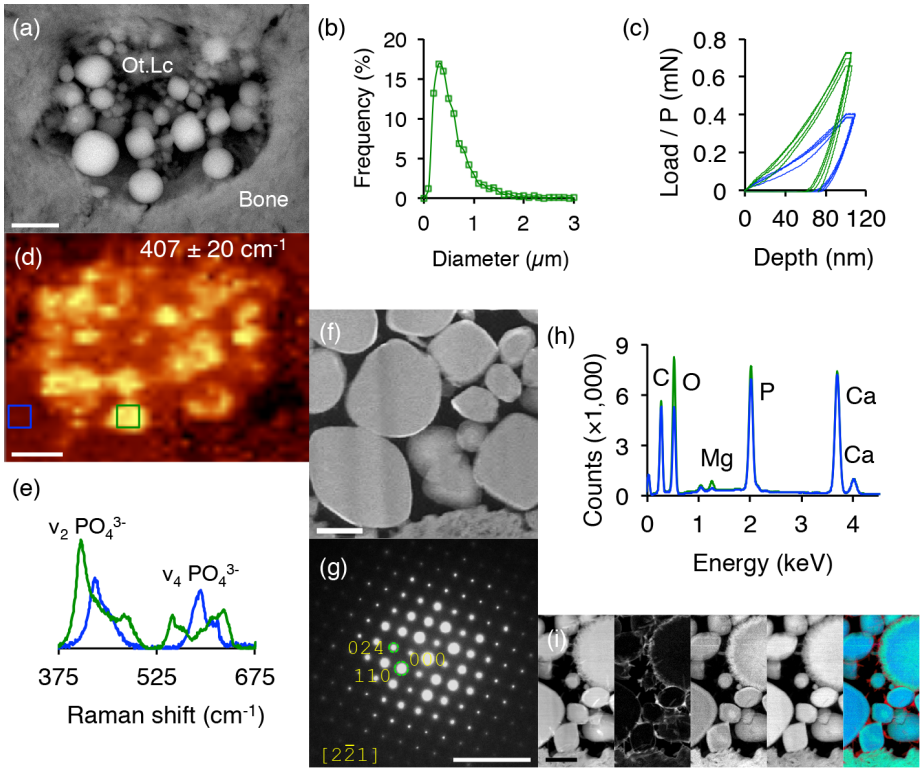

Figure 7. (a) A hypermineralised osteocyte lacuna (Ot.Lc) containing mineral nodules in BP bone (BSE-SEM). (b) Size distribution of mineral nodules. (c) Nanoindentation load-displacement curves (nodules = green; bone = blue). (d) Raman intensity map corresponding to the $v_2\ PO_4^{3-}$ peak at 407 cm^{-1}, indicating a whitlockite-like structure of mineral nodules. (e) Raman spectra corresponding to green (nodule) and blue (bone matrix) boxes shown in d. (f) HAADF-STEM image of mineral nodules. (g) SAED shows single-crystal nature of mineral nodules, identified as magnesium whitlockite. (h) EDX spectra showing Mg enrichment of mineral nodules. (i) EELS elemental maps. Left to right: HAADF-STEM, C, Ca, O, RGB colour-merge of C (red), Ca (green), and O (blue). Scale bars in a and d = 2 μm, f and i = 500 nm, g = 5 1/nm.

In *BP* bone, hypermineralised Ot.Lc contained equiaxed, ~80 nm to ~3 μm-wide, mineral nodules that were spherical to rhomboidal in morphology **(Figure 7)**. The internodular space was occupied by acicular nanocrystallites oriented randomly. Additionally, a distinct hypermineralised ring frequently surrounded the lacuna. Compared to the surrounding bone matrix, the mineral nodules had ~120% higher H and ~50% higher E_r. Raman spectroscopy indicated a whitlockite-like structure of these nodules with the ν_1 PO_4^{3-} symmetric stretching mode at ~970–972 cm^{-1} and the ν_2 PO_4^{3-} bending vibration at ~407 cm^{-1}. Typically for bone apatite, the ν_1 PO_4^{3-} band occurs at 958–960 cm^{-1} while the ν_2 PO_4^{3-} band is seen at ~432 cm^{-1}. HAADF-STEM also showed spherical and rhomboidal nodules that were strikingly facetted, and occasionally spherical nodules with a fuzzy exterior, a core-shell structure and nanoporosities distributed throughout the bulk. In agreement with the edge-on dimensions of extrafibrillar apatite platelets, 5–7 nm thick internodular acicular nanocrystallites were oriented heterogeneously. Collagen fibrils were not detected inside the lacunar space. The hypermineralised ring, also devoid of collagen fibrils, was 200–500 nm wide, comprised of small, closely packed nanocrystallites.

SAED showed that rhomboidal nodules were almost exclusively single-crystals of magnesium whitlockite. Spherical nodules were also highly crystalline. However, spherical nodules having a fuzzy exterior appeared polycrystalline. Internodular acicular nanocrystallites were apatite. In bone matrix, mineralised collagen fibrils oriented parallel to the image plane showed a preferred orientation of the (002) and (004) crystallographic planes, i.e., the *c*-axis, of bone apatite. Elemental analysis using SEM-EDX revealed higher Mg, P, and O content of the mineral nodules, and higher Mg/Ca but lower Ca/P ratios than bone matrix. Elemental mapping using STEM-EDX also showed Mg, P, and O enrichment of mineral nodules compared to bone matrix, internodular nanocrystallites, and the hypermineralised ring. EELS confirmed the lower Ca and higher O content of mineral nodules than bone matrix. Energy-loss near-edge structure of bone matrix showed higher amorphous carbon from the organic inclusions within nanoporosities and higher mineral carbonate.

In *Ctrl* bone, where individual mineral nodules could not be readily identified by BSE-SEM, hypermineralised Ot.Lc mainly contained acicular apatite nanocrystallites, oriented heterogeneously. Mg-enrichment of these nanocrystallites was negligible compared to bone matrix, seemingly similar to those occupying the internodular space in *BP* bone. These nanocrystallites occasionally stacked together to form dense aggregations.

4.3 Paper III

This work uses correlative microscopy to study physical connectivity between resin-filled canaliculi from osteocytes within autogenous bone fragments found in implantation sites and those in *de novo* formed bone on the fragment surface.

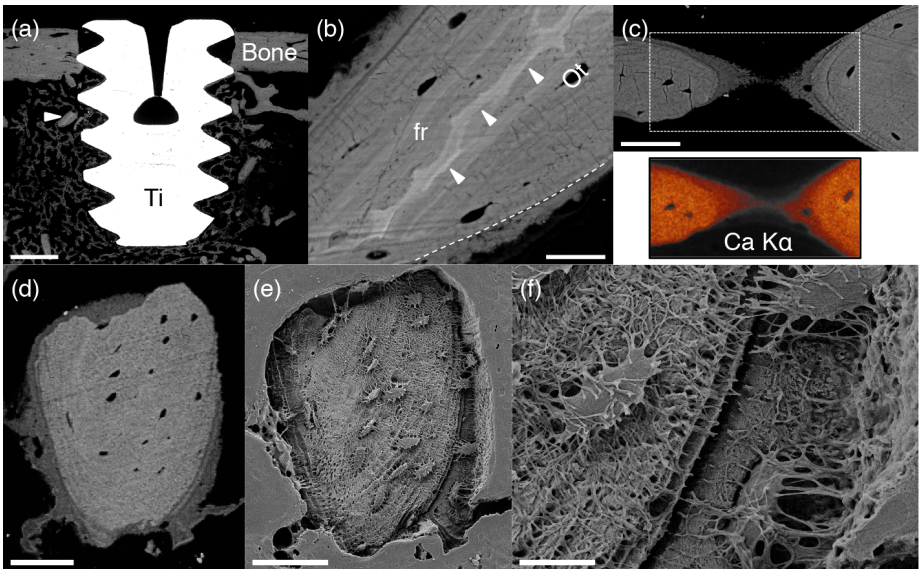

Figure 8. (a) Numerous autogenous bone fragments (arrowhead) in a healing implant site (BSE-SEM). (b) In the rat, fragments (fr) of original cortical bone can be identified by the presence of islands of unremodelled hypermineralised cartilage (arrowheads). The interface between the autogenous bone fragment and the newly formed bone on the surface is clearly demarcated (white broken line) by the difference in BSE Z- contrast. (c) The newly formed bone bridges the gap between two fragments. The elemental map represents the Kα X-ray emission line for calcium (Ca Kα) showing lower Ca content of the new formed bone compared to the old bone of the fragment. (d) An autogenous bone fragment that presents a large surface area for new bone formation. (e, f) Following resin cast etching, osteocytes in the autogenous bone fragment connect with those in the newly formed bone and thereby afford connectivity with the surrounding marrow space. Scale bars in a = 500 µm, b = 25 µm, c,d, and e = 50 µm, f = 10 µm.

Varying greatly in size and quantity, autogenous bone fragments are frequently observed around the implant and within the implant threads, in addition to rapidly formed woven bone, during the early healing stage **(Figure 8)**. In the laboratory rat, e.g., Sprague Dawley, such fragments of the original cortical bone are easy to identify by the inclusion of islands of unremodelled hypermineralised cartilage. Autogenous fragments are also found in close spatial association with rapidly forming woven bone. The extracellular matrix at different stages of mineralisation can be distinguished from the variation in BSE *Z*- contrast since younger (or less mature) tissue exhibits a lower *Z*- contrast, and therefore appears relatively darker since the local calcium content is lower.

In bone that forms on the surface of autogenous fragments, partially embedded osteocytes (osteoblastic-osteocytes) in the new forming bone are aligned parallel to the surface of the underlying fragment. The extracellular matrix deposited on the fragment surface therefore also appears well-aligned and ordered. The presence of sub-micron sized foci makes the mineralisation front appear granular. Where several fragments are found in close proximity to each other, the newly formed bone on the fragment surface tends to bridge the intervening gap.

The calcium and phosphorus content of the newly formed tissue on the fragment surface is lower than the old bone of the fragments, as determined by EDX elemental mapping.

As bone formation progresses, osteocytes within the autogenous bone fragments appear to physically interact with osteocytes in the *de novo* formed bone on the fragment surface. Moreover, canaliculi from the osteocytes within the old bone of the fragments extend beyond the original periphery of the fragment and into the newly forming tissue where they establish numerous connections with newer osteocytes.

Small autogenous bone fragments present a large surface area for new bone formation, attributable to the inverse relationship between particle size and surface-to-volume ratio. High coverage of the surface of fragment with newly formed bone is observed frequently. Even at an early healing stage, the newly formed bone occupies a large surface area with respect to the surface area of the fragment itself. Moreover, physical interaction between osteocytes resident within the old bone of the fragments and those in the newly formed bone, connectivity between osteocytes residing deep within the fragments and the surrounding marrow space is maintained.

4.4 Paper IV

This work evaluates the osseointegration of laser-modified, screw-shaped, cp-Ti implants after 8 weeks of healing in rabbits.

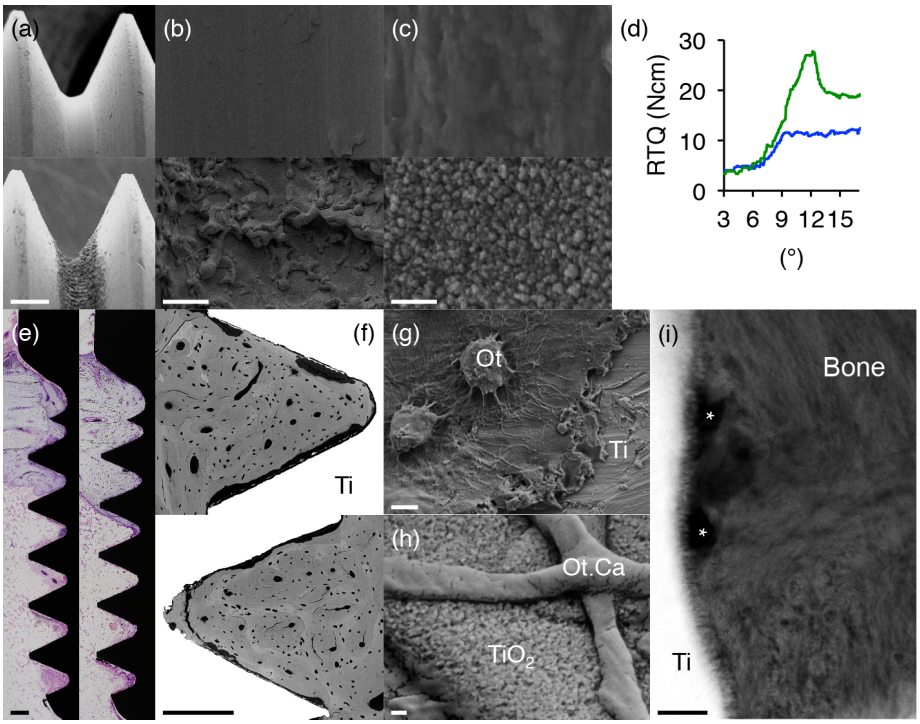

Figure 9. (a–c) Machined (top) and laser-modified (bottom) implants (SE-SEM). (d) Typical load deformation curves for the machined (blue) and laser-modified (green) implants. (e) Histology. Machined (left) and laser-modified (right) implants. (f) Machined (top) and laser-modified (bottom) implants showing highly mineralised bone within the threads (BSE-SEM). A fracture line is seen a short distance from the laser-modified thread valley. (g–h) Direct visualisation of osteocyte morphology. Osteocytes (Ot) are seen adjacent to the machined implant surface (g), whereas osteocyte canaliculi (Ot.Ca) are directly attached to the surface of the laser-modified implants (h). (i) HAADF-STEM image of the bone-implant interface at the laser-modified implants. Ot.Ca (asterisks) appear to make direct contact with the implant surface. Scale bars in a and f = 200 µm, b = 20 µm, c and h= 100 nm, e = 250 µm, g = 5 µm, i = 250 nm.

The surface oxide thickness, measured using AES, was 13.8 nm for the machined surface and 53 nm for the laser-modified surface. Compared to the relatively smooth machined implants, laser-modification resulted in a distinct hierarchical structure with a combined macro-, micro- and nanotopography **(Figure 9)**. The ISQ increased for both implant types between insertion and subsequent retrieval at 8 weeks healing. The laser-modified implants showed 153% higher in RTQ at break-point. The load deformation plot of the machined implants showed a moderately linear increase in torque followed by a plateau while the laser-modified implants showed a sharp increase in torque followed by a distinct break-point with a short or no plateau. On histological evaluation, both implant types showed endosteal downgrowth. Attributable to RTQ, fracture lines were observed 30–50 μm from the implant surface, exclusively in the thread valleys of the laser-modified implants. In contrast, the machined implants showed a separation between the implant surface and bone. Cortical and endosteal threads of both implant types contained mature osteonal bone. Remodelling sites were found both at the bone-implant interface and centrally in the bone filling the threads. Mature osteocytes were aligned parallel to the implant surface, often < 10 μm from the implant surface. Both implant types showed high total BIC and total BA. As observed by BSE-SEM, the newly formed bone within the implant threads was highly mineralised. Endosteal threads of both implant types mainly contained *de novo* formed bone, with comparable mineralised bone area (> 80%) and N.Ot/B.Ar (> 1000 mm^{-2}).

At the valley, flank, and outside the thread, Raman spectroscopy indicated similar mineral crystallinity, mineral-to-matrix and carbonate-to-phosphate ratios for both implant types. Following resin cast etching, osteocytes were seen in close proximity to the implant surface with canaliculi approaching the implant surface as well as Haversian canals. Mechanical disruption of the interface by RTQ precluded observation of canaliculi attached directly to the surface of machined implants. However, large numbers of branching canaliculi were found in close proximity to the nanotextured surface oxide layer of the laser-modified implants, extending several micrometres to approach globular features on the implant surface, forming an intercommunicating network adhering to the complex microtopography of the surface. HAADF-STEM imaging also showed a thick surface oxide layer having a distinct nanostructure. Collagen fibrils were aligned parallel to the implant surface, exhibiting the characteristic 67 nm cross-striated pattern. Canaliculi were observed at the immediate interface and at some distance from the surface oxide. Collagen fibril organisation was less regular adjacent to these structures. At high resolution, mineralised collagen fibrils appeared to interlock with the surface TiO_2 layer.

4.5 Paper V

This work explores nanoscale osseointegration of laser-modified dental implants retrieved after four years of clinical function.

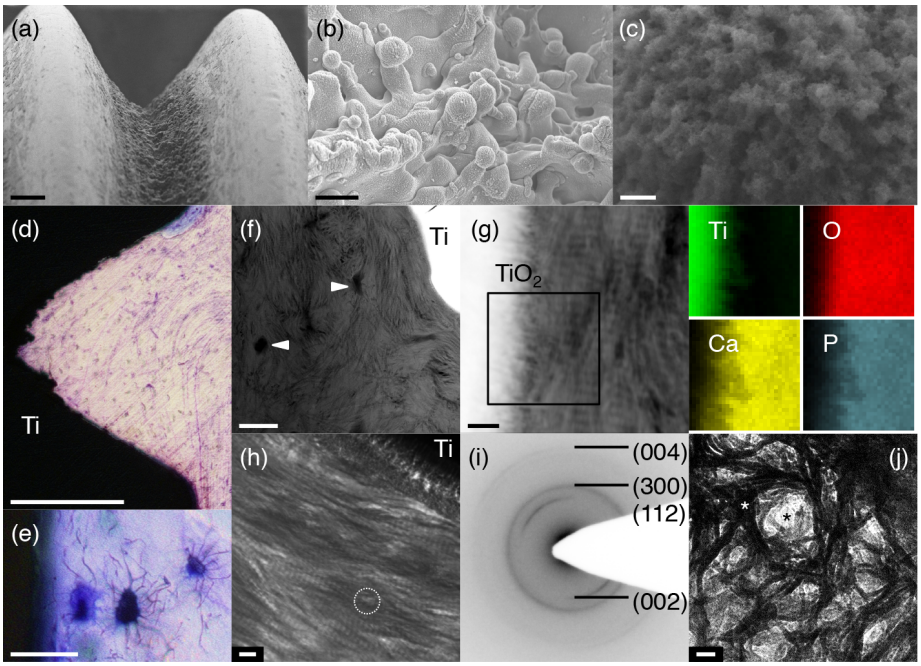

Figure 10. (a–c) Native, laser-modified implant surface (SE-SEM). (d) Mature lamellar bone fills the entire implant thread. (e) Osteocytes and canalicular networks close to the implant surface. (f) HAADF-STEM image of the bone-implant interface showing collagen aligned parallel to the implant surface. Several canaliculi are detected (arrowheads). (g) HAADF-STEM and STEM-EDX elemental maps corresponding to the location indicated by the black box. (h) TEM image of the bone-implant interface. (i) SAED pattern, obtained from the area shown as a white ring in h, demonstrates preferential alignment of apatite crystallographic c-axis with respect to the orientation of the collagen fibrils. (j) TEM image showing the open lacy structure of transversely sectioned collagen fibrils (black asterisk) tangentially surrounded by mineral platelets (white asterisk). Scale bars in a = 100 µm, b = 10 µm, c = 500 nm, d = 200 µm, e = 25 µm, f = 1 µm, g and h = 200 nm, j = 20 nm.

The native implant surface had a dual surface structure consisting of laser ablation tracks confined to the thread valley and as-machined areas of the upper part of the frank and the thread top **(Figure 10)**. The laser-ablated area showed globules (1–10 μm) of resolidified metal and distinct nanoscale irregularities. The surface morphology of the retrieved implants was evaluated by micro-CT and appeared similar to the native implant surface.

Due to damage to one of the implants during trephine retrieval, only two implants could be analysed. Histological evaluation showed large amounts of mature bone around and in direct contact with the implant surface, with many of the threads nearly completely filled with lamellar bone organised into Haversian systems. Close to the implant surface, concentric lamellae were aligned parallel to the implant surface. Osteocytes were oriented along the lamellar direction with canalicular networks directed perpendicular to the implant surface. Ongoing remodelling was evident. Histomorphometry demonstrated BA and BIC values in $> 80\%$ for both implants.

In HAADF-STEM, mineralised bone was seen in direct contact with the laser-modified surface. Collagen fibrils were oriented parallel to the implant surface up to 0.5–1 μm from the surface oxide. Collagen fibrils appeared to organise into 1–3 μm diameter concentric bundles and were detected as close as 100 nm from the implant surface, closely following the surface micro-topography. Circular features in the 200–400 nm size range, presumably canaliculi, were found 1–2 μm from the surface.

STEM-EDX showed an overlap of Ti, O, Ca, and P signals at the interface zone. Ti and O signal overlap indicates the surface TiO_2 layer, while Ti, Ca, and P overlap indicates a gradual intermixing of bone mineral with the surface oxide. Moreover, stoichiometrically relevant Ca/P ratios (1.33–1.67) for bone mineral were measured up to 800 nm from the implant surface. In some areas, an open, lacy structure comprised of ~59 nm × ~5 nm electron-dense mineral structures (Ca/P = ~1.33; C/Ca = ~1.33) interspersed between and 50–70 nm electron-lucent holes (C/Ca = ~3.33). SAED revealed a preferential alignment of the apatite crystallographic *c*-axis with respect to the orientation of collagen fibrils. The (002) and (004) reflections formed two arcs subtending angles of ~36° centred on the fibril direction. The (002) and (004) reflections were not observed for transversally sectioned collagen fibrils, indicating that these planes were oriented normal to the plane of the image.

4.6 Paper VI

This work investigates the osteocyte network adjacent to osseointegrated laser-modified dental implants, retrieved after four years of clinical function.

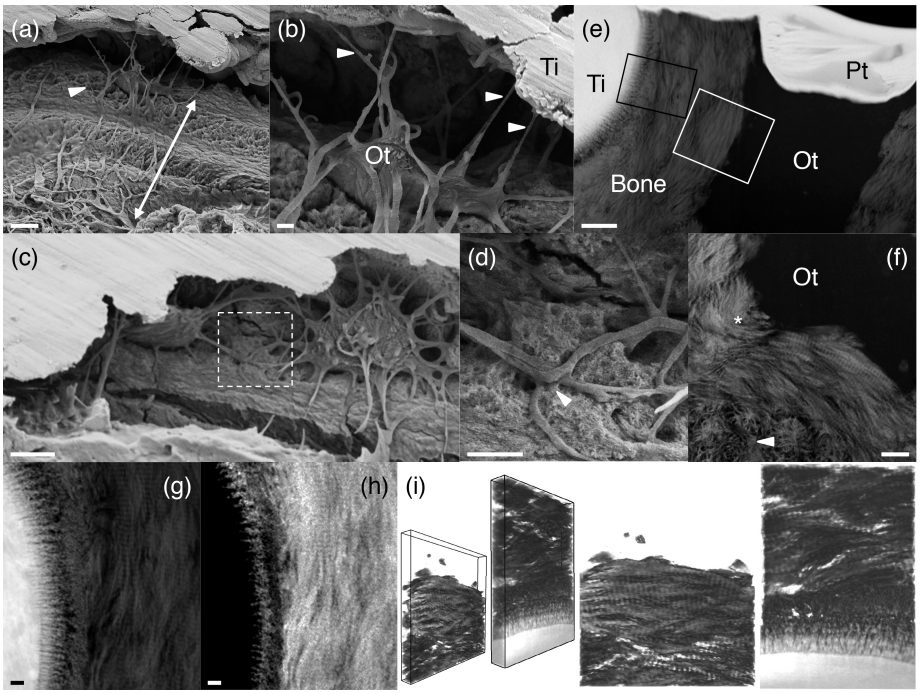

Figure 11. (a) Canaliculi from an osteocyte (Ot) extend toward the implant surface as well as in the direction of a central Haversian canal 30 µm away (arrowhead). (b) An osteocyte extends several canaliculi towards the surface oxide layer (arrowheads). (c) Area of new bone formation. Two osteocytes immediately below the bone surface have been exposed. (d) Interconnectivity of canaliculi from the two osteocytes (arrowhead), box in c, suggests cell-to-cell communication. (e) HAADF-STEM image showing organised bone between the implant surface and the osteocyte. (f) Bundles of collagen fibrils run parallel to the osteocyte surface. At a distance some run perpendicularly into the plane of the image (arrowhead). (g) Highly regular collagen banding adjacent to the implant surface. (h) EELS calcium map corresponding to g. (i) 3D electron tomography reconstructions of the bone-osteocyte interface (white box in e) and the bone-implant interface (black box in b). Scale bars in a = 5 µm, b and e = 1 µm, c = 5 µm, d = 2 µm, f = 500 nm, g, and h = 200 µm.

BSE-SEM revealed organised, osteonal lamellar bone around the implant and occupying the threads, with osteocytes aligned along concentric lamellae. The Ot.LCN, investigated by resin cast etching, connected the central Haversian canal to the implant surface through branching and rejoining canaliculi extending 30−50 μm **(Figure 11)**. Although the nearest osteocytes were 3−5 μm from the implant surface, interconnected canalicular networks extended towards the laser-modified regions and the as-machined regions along the implant surface. Intimate contact was observed between canaliculi and the nanotextured surface. Compared to bone located external to the implant thread, the higher N.Ot.Ca/Ot.Lc was noted close to the implant surface, therefore indicating *less aged* tissue adjacent to the implant surface. In an area of new bone formation, where osteocytes immediately below the bone surface were exposed, canaliculi extended towards the bone formation front, and interconnectivity between canaliculi from individual osteocytes was seen, suggesting direct cell-to-cell communication. Collagen fibril organisation in the zone between the implant surface and a nearby osteocyte lacuna was investigated using HAADF-STEM. Collagen fibrils were generally co-parallel to both the implant surface (bone-implant interface) and the osteocyte surface (bone-osteocyte interface), except in areas of canalicular extensions where collagen fibrils appeared to wrap around the canaliculus. At the bone-implant interface, collagen fibrils were laid down almost directly adjacent to the surface oxide nanostructures that serve as a template for apatite formation. EELS calcium signal mapping showed apatite ingrowth (~200 nm) into the nanostructured surface oxide, thus establishing a functionally graded interface between the nanostructured surface and bone. An interfacial collagen-free zone could not be identified.

Electron tomography and 3D reconstruction was performed for two volumes: (*i*) the bone-implant interface, and (*ii*) the bone-osteocyte interface. Collagen fibrils ran along the plane of the sample in both cases and were parallel to the implant surface as well as the osteocyte. Although collagen fibrils make an immediate boundary to the lacunar space at the bone-osteocyte interface, the bone-implant interface appears to be structurally graded with apatite interdigitation into the oxide layer followed by well-aligned collagen fibrils interfacing the surface, further confirming the EELS findings. Nevertheless, the general morphology at both interfaces is that of collagen fibrils having a unidirectional alignment, exhibiting a ropelike twisting motif within a collagen fibre bundle, typical of lamellar bone. SAED showed the *c*-axis of apatite platelets to be aligned approximately parallel to the long axis of collagen fibrils, as seen from the arcs formed by the (002) and (004) reflections centred on the major fibril direction, subtending angles of ~35°.

4.7 Paper VII

In this work, 3D printed solid and macroporous Ti6Al4V implants were evaluated after six months healing in sheep. The solid implants were machined to remove the EBM surface.

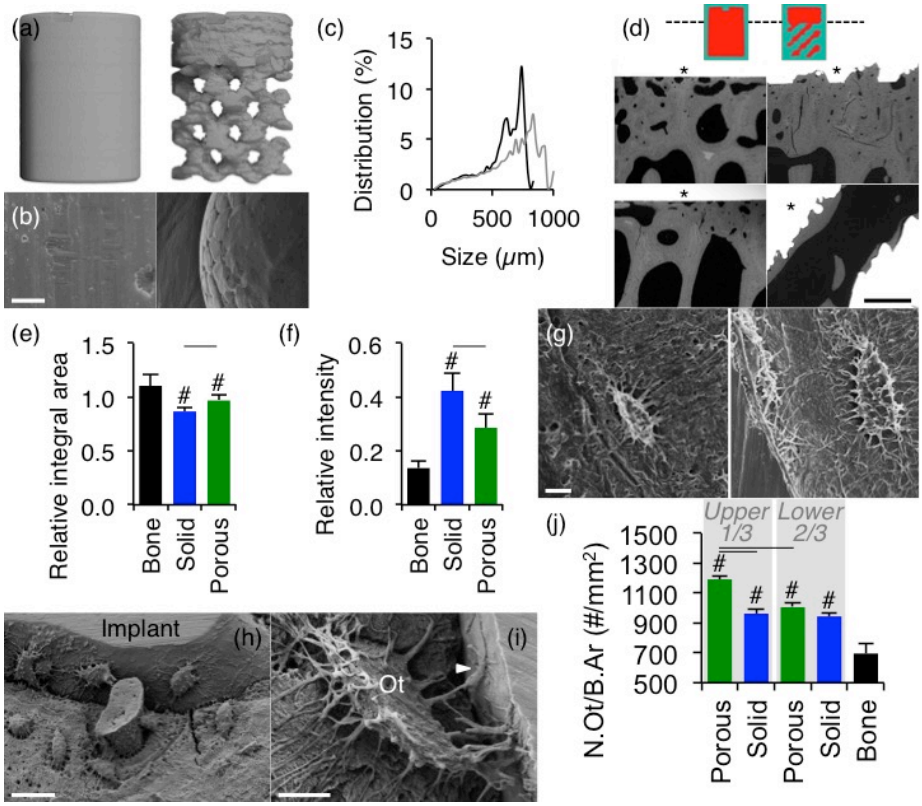

Figure 12. (a) Geometry of the solid and porous implants (micro-CT). (b) Surface of the solid (left) and porous (right) implants (SE-SEM). (c) Strut thickness (black) and separation (grey). (d) Illustration of the upper 1/3rd and lower 2/3rd regions of the implants. Bone formation adjacent to the upper 1/3rd (top row) and the lower 2/3rd (bottom row) regions of the implants (BSE-SEM). The implant surface is indicated by asterisks. (e) v_1 CO_3^{2-}/v_2 PO_4^{3-} ratio. (f) Phe/v_1 PO_4^{3-} ratio. (g) An osteocyte in native bone (left) appears considerably smaller with fewer canaliculi than an osteocyte adjacent to the implant surface (right). (h) Osteocytes in close positional association with vasculature and remain attached to the implant surface. (i) Canalicular attachment and branching (arrowhead) onto the implant surface. (j) Osteocyte density (N.Ot/B.Ar). # = statistical significance vs. bone; horizontal bar = statistical significance between the groups indicated.

The machined surface of the solid implants and the EBM surface of the porous implants exhibited surface areas of 1.098 mm^2 and 1.276 mm^2, respectively, per unit surface area (mm^2) of a theoretically smooth surface. The EBM surface is therefore 16.3% larger than the machined surface. The interconnected open-pore area of the porous implants comprised of ~583 μm thick struts with ~656 μm separations in between **(Figure 12)**. The open-pore area had a porosity of 62.7%. The interconnected struts had a total surface area of 249.1 mm^2, and a surface area/volume ratio of 6.84 mm^{-1}.

High levels of bone were observed around both implant types. Bone ingrowth into the interconnected open-pore area of the porous implants was demonstrated by micro-CT. BSE-SEM confirmed highly mineralised bone around both the solid and the porous implants. Bone ingrowth had also occurred into the open-pore area in the lower 2/3rd region of the porous implants. The lamellar pattern closely followed the surface contour, indicating that bone formation began at the implant surface and was directed progressively outward.

The mineral crystallinity and the mineral-to-matrix ratio of the interfacial tissue, at both implant surfaces, were similar to the native bone. The carbonate-to-phosphate ratio of the interfacial tissue at both implant surfaces was lower than the native bone, and higher for the porous implant than the solid implant. Pro, Phe, and Tyr signals were lower in the native bone than the interfacial tissue. Moreover, Phe and Tyr levels at the interfacial tissue were higher for the solid implants compared to the porous implants. For both implant types, interfacial tissue Ca/P ratio was lower than the native bone.

Osteocytes at the interface were aligned parallel to the implant surface and appeared to make intimate contact with the implant surface through numerous canaliculi. In close association with osteocytes and the implant surface, the presence of microvasculature was observed in the bone formed within the open-pore area of the porous implants. For both implant types, the N.Ot.Ca/Ot.Lc at the interfaces was similar, but 38–42% higher than the native bone. The N.Ot/B.Ar was higher at the interface for both implant surfaces, in both the upper 1/3rd and the lower 2/3rd regions. Overall, the N.Ot/B.Ar was higher at the porous implant surface than the solid implant surface. The N.Ot/B.Ar in the upper 1/3rd of the porous implants was higher than the lower 2/3rd (open-pore region) of the porous implants, as well as the upper 1/3rd of the solid implants. The N.Ot/B.Ar in the upper 1/3rd and the lower 2/3rd of the solid implant were comparable.

4.8 Paper VIII

In this work, 3D printed macroporous Ti6Al4V and CoCr implants were evaluated after six months healing in sheep.

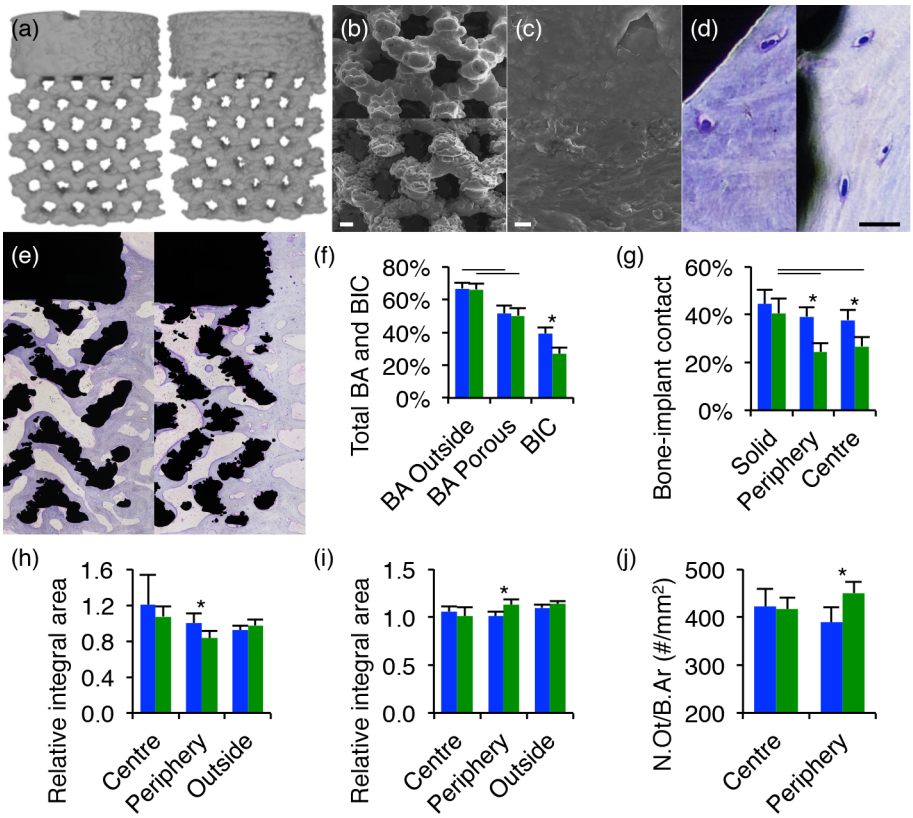

*Figure 13. (a) Geometry of the Ti6Al4V (left) and CoCr (right) implants (micro-CT). (b-c) Surface of the Ti6Al4V (top) and CoCr (bottom) implants (SE-SEM). (d) Histology. Mature lamellar bone in direct contact with the Ti6Al4V (left) and CoCr (right) surface. (e) Histology. Bone ingrowth into porous Ti6Al4V (left) and CoCr (right) constructs. (f) Overall histomorphometry. (g) BIC at different locations analysed inside and around the implants. (h) $v_2\ PO_4^{3-}$/Amide III ratio. (i) $v_1\ CO_3^{2-}/v_2\ PO_4^{3-}$ ratio. (j) Osteocyte density (N.Ot/B.Ar). f, g, h, i, j: Ti6Al4V = blue; CoCr = green. * = statistical significance between Ti6Al4V and CoCr; horizontal bar = statistical significance between the groups indicated.*

Ti6Al4V and CoCr implants had a similar open-pore structure, at 70% and 67% porosity, respectively **(Figure 13)**. The surface morphology of Ti6Al4V and CoCr implants was largely similar. Both Ti6Al4V and CoCr constructs were well integrated in bone. Mature trabecular bone was seen around the implants and extended into the porous network, and was directly in contact with the implant surface. The newly formed bone appeared morphologically similar to existing trabecular bone, with flattened osteocytes aligned parallel to the lamellar direction. Osteonal structures were observed close to the external surface, but not inside the porous network. Remodelling sites were observed at the bone-implant interface inside and outside the porous network. Both inside and outside the porous network, the BA was similar for both alloys, while the total BIC was higher for Ti6Al4V. The BIC for Ti6Al4V was higher than CoCr inside the porous network, but not at the solid top. At all locations (centre, periphery, close, distant), the BA was similar between Ti6Al4V and CoCr. For both Ti6Al4V and CoCr, the BA was highest close to the porous network and least at the centre.

The mineral crystallinity of the interfacial tissue at each location (centre, periphery, outside) was similar between Ti6Al4V and CoCr, however, CoCr showed lower mineral crystallinity at the centre and the periphery of the porous network compared to the outside. The mineral-to-matrix ratio and carbonate-to-phosphate ratios at the centre of the porous network and in the new bone outside the implant were similar between Ti6Al4V and CoCr. Phe and Tyr levels at the interfacial tissue were higher than outside the porous network, for both Ti6Al4V and CoCr. For CoCr, the mineral-to-matrix ratio at the periphery of the porous network was lower than Ti6Al4V, which was also lower than at the centre of the porous network and outside. The carbonate-to-phosphate ratio at the periphery of the porous network was higher for CoCr than Ti6Al4V, and was higher than at the centre of the porous network. The Ca/P ratio of the interfacial tissue, although similar for CoCr and Ti6Al4V, was lower than the native bone.

BSE-SEM showed well-mineralised bone containing blood vessels, remodelling sites, and osteocyte lacunae oriented along the lamellar direction. In areas of direct bone-implant contact, osteocytes were aligned parallel to the implant surface, and closely approached the Ti6Al4V and CoCr surfaces, forming interconnected networks, and often making direct contact with the surface of both alloys through canaliculi. N.Ot/B.Ar in the newly formed bone outside the porous network, and at the centre of the porous network was similar for Ti6Al4V and CoCr, but higher for CoCr (vs. Ti6Al4V) at the periphery of the porous network.

5 DISCUSSION

5.1 Osteocytes as indicators of bone quality

Osteocytes and the associated lacuno-canalicular network provide a great deal of information about the physico-chemical status of the surrounding bone. This is exemplified by the directional co-alignment of the principal axis of the osteocyte lacuna, and therefore also the osteocyte contained within, and apatite crystallites on the underlying bone surface [Paper I]. Although it has not been shown whether this relationship is disturbed, or otherwise affected, in compromised systemic conditions, it is apparent that the osteocyte lacuna is an important feature – one that is also aligned to the loading axis of bone [171, 172], and as such could have a role to play in distribution of mechanical forces. Another example is of the osteocyte lacuna undergoing mineralisation after osteocyte apoptosis, particularly in ageing human bone [56]. Mineralised osteocyte lacunae have also been reported in archaeological human bone and fossil mammal bone [173]. The pattern of mineralisation within osteocyte lacunae is not alike the mineralisation process observed during bone formation where mineral formation is under strict control of the organic matrix. In osteoporotic human alveolar bone obtained from women who had received anti-resorptive treatment, micrometre-sized spherical to markedly rhomboidal mineral nodules having a highly crystalline, magnesium whitlockite structure have been identified within mineralised lacunae [Paper II]. Here, not only is there a lack of physical constraints for the forming mineral due to the absence of collagen fibrils within the lacuna, but the formation of highly crystalline magnesium whitlockite, a calcium phosphate phase more stable than apatite at acidic pH levels, indicates significant changes in the local chemical environment. Such mineral nodules are stiffer and more resistant to plastic deformation than the extracellular matrix, resulting in altered local mechanical properties. A heightened prevalence of hypermineralised lacunae would thus contribute strongly towards the fragility of ageing bone [59]. The presence of hypermineralised lacunae thus implies local tissue deterioration. Yet another example is of the Ot.LCN, direct visualisation of which has also enabled understanding the fate of autogenous bone fragments generated inadvertently during implant site preparation [Paper III]. Autogenous bone fragments constitute a source of different growth factors affecting bone formation and resorption [174, 175], and provide osteoconductive surfaces within a healing bone defect. As new bone forms on the surface of such fragments, canaliculi can be seen extending between osteocytes in the new bone and those within the

original periphery of the fragment. This indicates that disrupted canalicular networks can be repaired, thus restoring communication channels between the fragment and the surrounding marrow space, thereby enabling the fragment to remain vital. The osteocyte lacuno-canalicular also shows certain morphological adaptations around bone anchored implants, e.g., increased osteocyte density, in response to mechanical loading [176].

Interpretation of the structure of the material-tissue interface is influenced by many factors. Of those, the importance of the analytical techniques used (and their limitations) and the associated sample preparation methods cannot be overstated, as they contribute greatly to different observations being made despite all other parameters being consistent. For instance, fixative solutions and embedding media can induce considerable amounts of tissue shrinkage and distort the lateral dimensions of osteocyte processes [177]. On the other hand, quantitative histomorphometry may indicate differences in the osteogenic potential of two sets of implant design features during early healing. One example that early differences may be maintained after longer healing periods is of thin hydroxyapatite coatings vs. uncoated cp-Ti [178, 179]. Nevertheless, such differences are often less obvious at intermediate and late healing where a steady state may have been attained between the rates of bone formation and remodelling. A key implication of such a steady state is that at intermediate and late healing time periods, minimal differences are to be expected in bone quality in relation to two *approximately* similar implant geometries. Given comparable healing conditions, the amount of bone formed would be similar for different implant surfaces, since the amounts of bone being deposited, being resorbed, and remaining mature and stable would be similar. This means that the overall composition of the extracellular matrix, and the osteocyte density would also be similar when the healing conditions are comparable, unless an implant surface is somehow able to exert its influence for long periods of time over large distances. An exception would be the immediate junction between the bone and the implant surface, where bone directly contacting the implant surface is thought to represent contact osteogenesis. This is frequently reported as the bone-implant contact. This junction is also important since osteocytes, formerly osteoblasts and precursor osteogenic cells, physically attach on to the implant surface through dendritic extensions called osteocyte processes, which reside within bony walls of the canaliculi. Although the early healing stage is critical for achieving osseointegration, the intermediate and late healing stages reflect the sustained impact, or lack thereof, of a given surface modification, implant geometry, and the bulk and surface physico-chemical characteristics of the implanted device. These concerns may be addressed by utilising advanced analytical approaches to measure specific parameters related to bone quality.

5.2 Selective laser ablation

In addition to achieving increased surface roughness through a contamination-free, site-specific process, titanium implant surfaces exhibit a dual micro- and nanoscale topography mimicking the hierarchical structure of bone [Papers IV–VI]. When ablated by a pulsed, 1024 nm Nd:YAG laser, cp-Ti undergoes changes in surface structure due to local heating, cooling, and crystallisation, resulting in a hierarchical micro- and nanoscale topography and a greatly enlarged surface area and altered surface chemistry. In the presence of ambient oxygen, temperature changes at the surface cause the surface oxide layer to increase in thickness from ~4–5 nm to ~100–500 nm, and transform into crystalline TiO_2 [180, 181].

The micrometre scale features are 1–10 µm globular structures resulting from melting and resolidification of the metal. These represent the *cellular* length scale and provide a large surface area for mechanical interlocking between bone and the implant surface. Superimposed onto these globular structures are nanoscale features comprised of a *channel-like* arrangement of a 50–300 nm thick TiO_2 surface layer that develops during cooling. These channels appear to be only a few nanometres, i.e., 5–20 nm, wide. Interestingly, self-assembled and vertically oriented TiO_2 nanotubes 15 nm in diameter are said to be considered optimal for focal adhesion and differentiation of mesenchymal stem cells [119], primary human osteoblasts, and haematopoietic stem cells [118].

At 8 weeks of healing in the rabbit [Paper IV], laser-modified implants exhibit greatly enhanced biomechanical anchorage than machined implants, as demonstrated by RTQ measurements. The load deformation pattern of laser-modified implants shows a sharp increase in torque that is followed by a distinct break-point and a brief plateau. In comparison, the load deformation pattern of machined implants shows a gradual increase in torque followed by a plateau. Structural evidence of higher RTQ and the unique load deformation pattern of the laser-modified implants is given by the appearance of fracture lines within the bone adjacent to the laser-modified area of the implant thread. The implication is that interfacial adhesion between the implant surface and bone is stronger than the strength of bone itself. However, the composition of the tissue formed adjacent to both implant types is largely similar, as evaluated by Raman spectroscopy, indicating that laser-modification of the implant surface does not affect extracellular matrix production and mineralisation. Furthermore, similar osteocyte densities for the two implant types provide further evidence that laser-modification of the implant surface does not alter bone formation kinetics. However, direct

visualisation of the Ot.LCN showed that osteocytes align parallel to the implant surface and in fact make a direct contact with the surface of the laser-modified implants via numerous canaliculi. This was apparent despite the disruption of the bone-implant interface during RTQ measurements. On the other hand, a thin layer of embedding resin almost always separated osteocytes from the surface of the machined implants. Although RTQ measurements may have exaggerated this separation, a layer of embedding resin has been demonstrated previously between bone and the machined implant surface, where RTQ measurements had not been performed [182]. HAADF-STEM imaging of the laser-modified surface showed mineralised collagen fibrils in close association with the implant surface and aligned parallel to it. Canaliculi were also observed to make direct contact with the implant surface.

To validate the role of laser-modification in improving biomechanical anchorage, a correlative assessment of bone interfacing functionally loaded implants retrieved from the human maxilla after 47 months was undertaken [Paper V and VI]. These implants were explanted because of mechanical failure of the implant material, rather than biological failure, e.g., implant loosening due to lack of osseointegration or loss of osseointegration due to periimplantitis. The observed BA and BIC values (> 80%) are in agreement with those acquired for clinically stable, machined dental implants of a similar design retrieved from four patients (aged 52–70 years) after 1–16 years of clinical function where BIC of 56–85% and BA of 79–95% were reported for seven implants [183].

As also observed in the rabbit model, osteocytes in close proximity to the implant surface extended canaliculi towards the implant surface that were seen as 200–400 nm diameter structures within a couple of micrometres from the surface. In bone, the canalicular network provides a framework for exchange of information [184]. Similarly, it is likely that the direct connectivity between osteocyte canaliculi and the implant surface represents the architecture facilitating information exchange between osteocytes found in the interfacial bone and the implant surface [Paper VI]. Importantly, after nearly four years of clinical function, the intricate surface oxide layer remains intact. While it cannot be said for certain whether the osteocyte processes within the canaliculi are indeed attached to the surface oxide, it is plausible that the close attachment of osteocyte processes to the implant surface is meant to serve a specific function, whether it is one of anchorage [185, 186] or to sense mechanical stimuli as strain [49, 187] or vibrations [188]. Lack of mechanical stimulation is understood to be related to increased osteocyte apoptosis and loss of cell viability [189]. Using a similar resin cast etching technique, a

reduction in the average number of canaliculi per osteocyte lacuna has been reported with advancing tissue age, implying reduced connectivity between osteocytes and the surrounding tissue [184]. From a biomechanical perspective, the implants studied in this work had been in functional use for nearly four years while supporting excessively high loads associated with parafunctional grinding of the teeth or clenching of the jaw – a condition called *bruxism* [Papers V–VI]. The lamellar pattern of bone adjacent to the implant surface indicates that the direction of bone formation is normal to the implant surface, where presumably the differentiating osteogenic cells make contact with the implant surface, and begin to produce *de novo* bone by contact osteogenesis, to later become entrapped within the surrounding bone as they terminally differentiate into osteocytes. The continued presence of osteocytes at the bone-implant interface further attests to the potential role that osteocytes play in maintaining an intact interface between an implant and mineralised bone, which remains adaptive to applied loads long after initial osseointegration has occurred.

The observation of well-aligned collagen fibrils directly abutting the implant surface after long-term clinical function are in agreement with observations made previously in human, where unloaded, laser-modified dental implants retrieved from the mandible of a 66-year-old male showed BIC of 31–32% and BA of 25–31% after only two and a half months of submerged healing [190]. The close spatial association between mineralised collagen fibrils and the implant surface provides strong evidence in disagreement with the *collagen-deficient*, cement line matrix description of the bone-implant interface [100]. On the other hand, deposition of calcium within the thickened surface oxide layer of laser-modified implants might seem analogous to the cement line matrix that is presumed to be collagen-free. However, collagen exclusion from these nanoscale features is primarily due to spatial constraints. The organisation of mineralised collagen fibrils into 1–3 μm wide bundles close to the implant surface appears similar to mineralised bundles seen on the bone surface after deproteinisation [Paper I]. While collagen is well-aligned adjacent to the implant surface, the arrangement of collagen fibrils around canaliculi is less ordered [13].

Earlier experimental studies have demonstrated enhanced biomechanical anchorage of similarly prepared laser-modified implants. When laser-modified in the lower 30% of the implant thread, 250% higher torque was required to cause anchorage failure of cp-Ti [129] and Ti6Al4V [181] implants after 8 weeks of healing in rabbits. Furthermore, at 6 months of healing in rabbits, the torque necessary to disrupt the bone-implant interface for laser-modified cp-Ti implants remained 170% higher than machined cp-Ti

implants [180]. Histological assessment revealed fracture lines in bone, a few micrometres from the implant surface in the laser-modified regions of cp-Ti [129] and Ti6Al4V [181] implants at 8 weeks, and cp-Ti implants at 6 months healing [180], in rabbits. Moreover, on the ultrastructural level, mineralised collagen fibrils were found directly bordering the thickened surface oxide layer of laser-modified cp-Ti [191] and Ti6Al4V [181] implants at 8 weeks, and cp-Ti implants at 6 months healing [180]. These findings were corroborated by observations made in 3D using HAADF-STEM tomography [167, 192].

At 8 weeks healing in rabbits, a number of characteristic ions have been identified at the bone-implant interface of laser-modified cp-Ti implants using Time-of-Flight Secondary Ion Mass Spectroscopy. These include $CaOH^+$, Ca_2O, $Ca_2O_2H^+$, $Ca_2PO_3^+$, $Ca_3O_3H^+$, $Ca_2PO_4^+$, and $Ca_3PO_5^+$ representing calcium phosphate signals originating from regions of mineralised bone, and CH_4N^+ (glycine), $CH_5N_3^+$ (arginine), $C_4H_8N^+$ (arginine/proline), $C_4H_{11}N_2^+$ (arginine), $C_5H_8N_3^+$ (histidine) representing protein signals originating from areas of bone formation or remodelling. Other signals include $^{46}Ti^+$, $^{47}Ti^+$, $^{48}Ti^+$, $^{49}Ti^+$, $^{50}Ti^+$ $^{46}TiO^+$, $^{47}TiO^+$, $^{48}TiO^+$, $^{49}TiO^+$, and $^{50}TiO^+$ representing titanium dioxide, and various triglyceride signals originating from structures identified as Haversian canals [191].

At 6 months healing in rabbits, an intimate contact is maintained between the surface oxide layer of the laser-modified cp-Ti implants and the mineralised tissue, with collagen fibrils aligned parallel to the implant surface [180]. Spacing measurements of lattice fringes in high-resolution TEM revealed crystalline apatite immediately outside the surface oxide layer, while STEM-EDX demonstrated a concentration gradient of calcium, phosphorus and oxygen across the interface [192]. In living tissues, graded interfaces are observed regularly between dissimilar materials and provide functionality, for example load-bearing capacity at tendon-bone [193] or the cartilage-bone interface [194].

5.3 Electron beam melting

3D printing techniques for metals and alloys, such as EBM, provide several key advantages over conventional machining. These include the possibly to fabricate constructs having an open-pore architecture to achieve bone ingrowth, and therefore enhanced mechanical anchorage of such implants. Pores must however be large enough to allow removal of debris after the build. Importantly, the overall geometry of a construct can be finely controlled.

Reduction in the stiffness or axial rigidity of a construct can potentially reduce the extent of stress-shielding experienced by bone around metal or alloy devices [137, 145, 195], which may be achieved by using an open-pore design. Measured by nanoindentation, the elastic moduli of human cortical and trabecular bone are ~20 GPa and ~18 GPa, respectively [196]. In comparison, the elastic moduli of Ti6Al4V (ASTM F136) and CoCr (ASTM F75) are ~114 GPa and ~220 GPa, respectively. The overall design of a construct can be tailored such that the mechanical properties match those of cortical bone, yet retaining high strength for use in high load bearing conditions, e.g., as orthopaedic implants.

3D printing of Ti6Al4V and CoCr by electron beam melting offers a key advantage in tailoring the construct design, e.g., the strut thickness, to lower the structural stiffness and match the elastic modulus of bone and therefore reduce stress shielding [130]. The surface of EBM manufactured constructs typically resembles the powder used in the process. Therefore, while half molten 50–100 μm particles contribute to a considerable increase in the overall surface area, the particles are much larger than eukaryotic cells, and are smooth on the submicron and nano- levels due to the atomisation process through which they are produced. For these reasons, it may be that the particle surface does not play a significant role in modulating cellular behaviour directly. However, the greatly increased surface area provides a greater surface area for cellular recruitment and attachment, and bone formation, while surface irregularities could favourably influence the mechanical retention of such devices in bone.

It is possible to *remove* the EBM surface consisting of half molten particles from the accessible exterior of a construct by machining [140]. Alternatively, the native surface of the porous construct including the interior can be modified through various surface treatments [197] to further enhance osseointegration. A direct comparison between EBM manufactured implants, with and without the EBM surface, demonstrates a considerably higher osteocyte density in the newly formed bone adjacent to the EBM surface, which may be related to the recruitment of greater numbers of osteoprogenitor cells, leading to a greater incidence of osteoblast entrapment and differentiation into osteocytes. Moreover, the EBM surface, compared to the machined surface, promotes tissue maturation, as reflected by an increased carbonate-to-phosphate ratio of the extracellular matrix. Importantly, the presence of vasculature within open-pore areas indicates that the bone formed here retains the capacity for nutrient exchange and removal of metabolites, and also the possibility for the migration of precursor cells

responsible for bone resorption and remodelling, as may be expected external to these open-pore areas [Paper VII].

Formation of woven bone [198] and subsequent remodelling [199] are local processes that represent the adaptive response of bone to dynamic loading. Interfacial stress transfer between a metal implant and bone depends on various combinations of compressive, tensile, and shear stresses at different locations along the surface of the implant [195]. A critical limitation of the present work is that the implants were not subjected to direct functional loading, and therefore the reduction in the extent of stress shielding experienced by bone due to an open-pore design cannot be estimated [Paper VII]. On the other hand, histomorphometric evaluation of Ti6Al4V and CoCr implants of approximately similar macro-geometry provides useful information about the biomechanical environment. Notably, the amounts of bone formed in response to Ti6Al4V and CoCr were similar irrespective of location, i.e., inside and outside the porous network. Moreover, the BIC was similar for CoCr and Ti6Al4V at the solid top region outside the porous network. In contrast, inside the porous network, CoCr exhibited lower BIC than Ti6Al4V, as well as lower BIC than outside the porous network. Since mechanical stimulation of the healing sites under physiological loading cannot be discounted, it is plausible that biomechanical environments inside and outside the porous network are distinctly dissimilar even under physiological loading conditions. As predicted by the Gibson & Ashby relationship [200], the stiffness of porous constructs is related to their relative density. The difference between the stiffness of Ti6Al4V and CoCr scales by a factor of two – CoCr being twice as stiff than Ti6Al4V [134]. Therefore, attributable to the difference in the overall stiffness of Ti6Al4V and CoCr constructs, the extent of stress transfer into bone inside the porous network may also not be equivalent for the two alloys. Bone may experience a greater extent of stress shielding inside the porous network than outside, particularly more so in the case of CoCr than Ti6Al4V. The difference in the local biomechanical environment is exaggerated at the periphery of the porous network, where the osteocyte density is higher, the mineral-to-matrix ratio is lower, and the carbonate-to-phosphate ratio is higher for CoCr than Ti6Al4V. Nevertheless, osteocytes make direct contact with the surface of both Ti6Al4V and CoCr, indicating that CoCr is indeed biocompatible and supports bone formation by contact osteogenesis.

Accurate morphometric assessment of *in vivo* performance of porous metal constructs remains a formidable task. Preparation for histological assessment results in up to 15% volumetric shrinkage [201]. Non-destructive techniques such as lab-based micro-CT allow assessment of bone ingrowth into

Ti6Al4V, but the direct bone-implant contact is often difficult to measure accurately or reproducibly, due to artefacts such as beam hardening and scatter [202]. This is perceived to be an even greater challenge when using alloys of a higher density, e.g., CoCr. Furthermore, smaller structures such as osteocyte lacunae can be difficult to identify, and their investigation is better suited to higher resolution techniques such as BSE-SEM, in 2D [163], and synchrotron radiation micro-CT, in 3D [172].

By keeping total porosity within a narrow range, e.g., 65–70%, pore dimensions can be varied [203], or vice versa, it is possible to identify the ideal combination of pore size and percentage porosity for optimal biomechanical anchorage and bone ingrowth.

Finally, as is true for all 3D printing technologies applicable to the production of implantable medical devices, EBM can be used to fabricate patient-specific implants. 3D printed, Ti6Al4V osteosynthesis plate has been used to secure a microvascular fibula flap in the reconstruction of the mandible [204]. Similarly, EBM has been successfully taken advantage of in the reconstruction of the mandible in an 84-year-old female [133].

5.4 Osteocytes and the bone-implant interface

Osteocytes, by virtue of their morphology, provide useful information regarding the state of native bone in normal and disease states. Likewise, osteocytes provide important information pertaining to the state of bone formed adjacent to metal or alloy implants. For instance, the average number of canaliculi per osteocyte lacuna tends to be higher adjacent to implant surfaces, compared to the native bone [Papers V and VII]. This is primarily related to tissue age, since bone adjacent to an implant surface will always be *less aged* compared to the native bone, in the same individual. However, what this suggests is that the interfacial tissue is vital tissue that is continually renewed, as dictated by the biomechanical environment next to the implant surface. This is further supported by interfacial tissue composition. For example, at six months of healing in sheep, the mineral-to-matrix ratio of the interfacial tissue is approximately similar to the native bone (> 1.5 mm from the Ti6Al4V implant surface) [Paper VII] and newly formed bone (300–700 μm from the Ti6Al4V implant surface) [Paper VIII].

Osteocytes express a diverse set of genes whose functions range from regulation of mineralisation (*DMP1*, *SOST*), to phosphate homeostasis (*PHEX*, *MEPE*, *FGF23*), and cytoskeletal arrangement and/or dendrite formation (*E11*, *CD44*, *CapG*, *Cdc42*, and *destrin*) [205]. In comparison, when

available in adequate concentrations, and where other conditions such as pH are favourable, the formation of biominerals such as apatite, is entirely thermodynamically driven. For instance, geological apatite forms entirely independent of cellular intervention and retains a high degree of long-range order, i.e., mineral crystallinity [32]. Therefore, if cells (i.e., osteoblasts initially, and osteocytes later) had little or no role to play in controlling the mineralisation process, either by the production of the organic matrix in an organised manner or by the production of mineralisation inhibitors such as alkaline phosphatase, it would not be uncommon to find hypermineralised regions (i.e., significantly elevated mineral-to-matrix ratio) adjacent to the implant surface. The argument, therefore, is that at intermediate and/or long healing periods, osteocytes have an active role to play in the continued maintenance of osseointegration.

It is not possible to directly visualise the osteocytes or their dendritic extensions by the resin cast etching technique [162]. In fact, the embedding resin infiltrates the pericellular space while the cellular components remain encapsulated inside. In the case of the Ot.LCN, the resin occupies the pericellular fluid space between the cell (or the dendrite) and the surrounding bony wall. Therefore, the observed resin filled structures approximate the inner dimensions of the lacuno-canalicular system, rather than those of the cells themselves. Indeed, certain conditions, for instance hypoxia and skeletal micro-damage may induce osteocyte apoptosis and/or the disruption of osteocyte processes. In such cases, although the cells and their dendritic extensions may be affected, the resin casts of the network remain approximately intact [206]. Moreover, although with the use of this technique, no evidence can be provided regarding whether the osteocyte processes were actually within the canaliculi, it may be assumed that the visualised osteocytes would include viable osteocytes as well as a certain unknown proportion of osteocytes in various stages of ageing and apoptosis, which can be confirmed by complementary histological assessment.

6 CONCLUSIONS

–Nanoscale mineral platelets at the osteoblastic-osteocyte lacuna (Ot.Lc) floor are aligned approximately parallel (within 0°–45°) to the long axis of the Ot.Lc. The mean orientation of mineral platelets at the Ot.Lc floor was 19° in the tibia and 20° in the femur. The majority of Ot.Lc exhibit a mean orientation of mineral platelets in the 0°–25° range [Paper I].

–Post-apoptotic mineralisation of the osteocyte lacuna in bisphosphonate-exposed human alveolar bone involves the formation of ~80 nm to ~3 µm wide, facetted, magnesium whitlockite crystals and consequently altered local mechanical properties, in addition to randomly oriented acicular apatite nanocrystallites distributed in between [Paper II].

–Autogenous fragments contribute towards osteogenesis within healing surgical defects, e.g., in the vicinity of bone-anchored implants. Such fragments contain osteocytes that are able to restore physical connectivity with osteocytes (osteoblastic-osteocytes) in *de novo* formed bone on the surface of such fragments, through canaliculi that contain cytoplasmic extensions of osteocytes [Paper III].

–Compared to machined implants, laser-modified implants exhibit greater biomechanical anchorage, and a distinctly different load deformation pattern. The BIC, BA, extracellular matrix composition, and osteocyte densities are similar for machined and laser-modified implants [Paper IV].

–Functionally loaded, nano-textured, laser-modified cp-Ti implants promote bone formation and remodelling, resulting in a functionally graded interface characterised by a gradual intermixing of bone with the thickened surface oxide layer [Paper V]. Furthermore, through canaliculi, osteocytes can make and retain intimate contact with implant surfaces and follow the contour of the implant surface even after extended healing periods in functionally loaded conditions [Paper VI].

–Compared to the machined surface, the EBM surface promotes bone healing, as evident from the carbonate, phenylalanine, and tyrosine content at the bone-implant interface. Furthermore, the EBM surface retains a higher number of osteocytes, indicating a greater capacity for sensing mechanical loading [Paper VII].

–Bone ingrowth can be achieved into open-pore CoCr constructs fabricated by EBM. Although Ti6Al4V shows higher BIC than CoCr, bone formation patterns around and inside open-pore CoCr and Ti6Al4V are comparable. While CoCr does not induce gross changes in the extracellular matrix composition at the centre of the porous network and outside the porous network, differences in the carbonate and phosphate content, as well as a higher osteocyte density at the periphery of the porous network, compared to Ti6Al4V, suggests differences in the local biomechanical environment attributable to the greater stiffness of CoCr [Paper VIII].

Whether from the shape of the lacunar space while the cell is undergoing a transformation from a surface osteoblast to a matrix-embedded osteocyte, or by the constituents of the lacunar space long after the cell has undergone apoptosis, osteocytes reveal important information about the relative age of the local tissue. Moreover, their presence on the surface of bone fragments, generated unintentionally during implant site preparation, attests not only in favour of the osteogenic potential of these fragments but may also indicate whether cells within such fragments are viable or not. Furthermore, morphological parameters such as size, alignment with respect to bone lamellae, prevalence, proximity to small and large blood vessels, or lacuno-canalicular interconnectivity between neighbouring and distant osteocytes, all disclose subtle clues regarding the status of bone as tissue regeneration occurs in the vicinity of, and in response to, implanted biomaterials. In terms of alignment and organisation of the building blocks of bone, i.e., mineralised collagen fibrils, ultrastructural similarities between the bone-osteocyte interface and the bone-implant interface indicate that certain metals and alloys indeed tend to elicit bone bonding and remodelling similar to normal bone development. Overall, while osteocytes are indicators of bone quality, they are important structural markers of osseointegration and can prove extremely beneficial in characterising the bone response to currently available materials as well as novel materials for load bearing applications in dental rehabilitation and orthopaedics.

7 FUTURE PERSPECTIVES

The findings reported in this thesis validate the importance of the Ot.LCN in interpreting the physico-chemical status of bone. Through the use of hierarchical imaging techniques and a range of complementary spectroscopy techniques, various structural parameters have been identified that correspond to phases of bone formation, remodelling, and ageing. Specifically in the context of bone anchored metal implants, it would be pertinent to explore further the following:

–The ultrastructure of the interface, i.e., arrangement of collagen fibrils and apatite, and the dynamics of bone formation and remodelling to a given set of implant design features in different compromised conditions, e.g., diabetes or irradiated tissues.

–The effect of ultrastructural organisation on the resulting function, e.g., mechanical load transfer.

–Distinguishing between contact osteogenesis and other sources of bone formation within a healing defect, i.e., distance osteogenesis, woven bone, and autogenous bone fragments, to determine the absolute osteogenic potential of various implant design features.

–Adaptation of the Ot.LCN adjacent to physiologically or externally loaded implants of varying bulk moduli but similar external dimensions, surface chemistry, and topography.

–Gene expression of osteocytes with respect to distance from the implant surface under external loading and physiological loading.

ACKNOWLEDGEMENTS

It has been a great privilege to be involved in such a truly unique, multiscale project, and I wish to thank everyone who has directly or indirectly contributed to this incredible journey.

First of all, I would like to express my sincere gratitude to my main supervisor, Anders Palmquist whose ideas, thoughts, guidance, encouragement, and availability have been instrumental in realising this project. You have taught me how to visualise the bigger picture, macroscopically, and make finer adjustments, on the micro- and nano- levels, and see outside the box, in 2D and 3D. Besides science, there have also been incredible adventures from shopping in Tokyo, witnessing history in Krakow, to watching Major League Baseball in Toronto, as well as many astonishing sleight-of-hand card tricks. Thank you for always believing in me.

I also would like to thank my co-supervisors, Peter Thomsen and Aleksandar Matic for giving me every opportunity to pursue my ideas, for allowing me to work both independently and within other projects. I am always amazed at your unique perspectives. Thank you for showing me how to think critically. I am extremely grateful for your unfaltering support and encouragement.

I wish to thank Maria Utterhall and Magnus Wassenius for always having the perfect solutions for all practical and administrative matters; and Lena Emanuelsson and Birgitta Norlindh for sharing your knowledge, all the unheard all-revealing stories from the yesteryears, recipes, and of course your technical expertise.

A massive thanks to all my co-authors: Kathryn Grandfield, Xiaoyue Wang, James Tedesco, Bryan Lee, Patrik Stenlund, Margarita Trobos, Felicia Suska, Omar Omar, Rickard Brånemark, Anders Snis, Jukka Lausmaa, Cecilia Persson, Martin Johansson, Hanna Simonsson, Cecilia Larsson Wexell, Lena Emanuelsson, Birgitta Norlindh, Anna Martinelli, Ezio Zanghellini, Bengt Nilson, and Bengt Johansson.

I am especially grateful to all friends, and present and former colleagues: Ibrahim Elgali, Magdalena Zaborowska, Annika Juhlin, Xiaoqin Wang, Sara Svensson, Shariel Sayardoust, Forugh Vazirisani, Patrik Stenlund, Carina Cardemil, Maria Lennerås, and Necati Harmankaya.

A special thanks to Kathryn, James, Bryan, and Dan for the fabulous time at the Canadian Centre for Electron Microscopy in Hamilton, and Cecilia Persson for hosting me at the Ångstrom Laboratory in Uppsala.

I wish to thank Maria Hoffman and Anna Johansson for sharing their knowledge of cell culture techniques; Ezio Zanghellini and Katarina Logg for teaching me the practical aspects of Raman spectroscopy; and Stefan Gustafsson and Anders Kvist for patience towards my endless queries.

I also want to thank other professors; Eva Olsson, Christer Dahlin, Pentti Tengvall, and Tomas Albrektsson for their kindness and wisdom.

And finally, Eman, my best friend in the whole world, who has always believed in me and in my abilities, has supported me through the best of times and the worst of times, and has always been caring, understanding, and appreciative. Words are not enough. Thank you for being my rock!

Financial support was received from the Swedish Research Council (grants K2012-52X-09495-25-3 and K2015-52X-09495-28-4), the BIOMATCELL VINN Excellence Center of Biomaterials and Cell Therapy, the Region Västra Götaland, the ALF/LUA research grant “Optimization of osseointegration for treatment of transfemoral amputees” (ALFGBG-448851), the IngaBritt and Arne Lundberg Foundation, the Wilhelm and Martina Lundgren Vetenskapsfond, the Dr Felix Neubergh Foundation, Promobilia, and the Hjalmar Svensson Foundation, Oticon Medical AB, and the Swedish Government Strategic Funding of Materials Science Area of Advance, provided to Chalmers and Department of Biomaterials, University of Gothenburg.

REFERENCES

1. Fratzl P, Weinkamer R. Nature's hierarchical materials. Prog Mater Sci. 2007;52:1263-334.
2. Seeman E, Delmas PD. Bone Quality — The Material and Structural Basis of Bone Strength and Fragility. N Engl J Med. 2006;354:2250-61.
3. Meyers MA, Chen P-Y, Lin AY-M, Seki Y. Biological materials: Structure and mechanical properties. Prog Mater Sci. 2008;53:1-206.
4. Meyers MA, McKittrick J, Chen PY. Structural biological materials: critical mechanics-materials connections. Science. 2013;339:773-9.
5. Weiner S, Wagner HD. The Material Bone: Structure-Mechanical Function Relations. Annu Rev Mater Sci. 1998;28:271-98.
6. Reznikov N, Shahar R, Weiner S. Bone hierarchical structure in three dimensions. Acta Biomater. 2014;10:3815-26.
7. Nudelman F, Pieterse K, George A, Bomans PH, Friedrich H, Brylka LJ, et al. The role of collagen in bone apatite formation in the presence of hydroxyapatite nucleation inhibitors. Nat Mater. 2010;9:1004-9.
8. Wang Y, Azais T, Robin M, Vallee A, Catania C, Legriel P, et al. The predominant role of collagen in the nucleation, growth, structure and orientation of bone apatite. Nat Mater. 2012;11:724-33.
9. Boskey AL. Matrix proteins and mineralization: an overview. Connect Tissue Res. 1996;35:357-63.
10. Landis WJ, Hodgens KJ, Song MJ, Arena J, Kiyonaga S, Marko M, et al. Mineralization of collagen may occur on fibril surfaces: evidence from conventional and high-voltage electron microscopy and three-dimensional imaging. J Struct Biol. 1996;117:24-35.
11. Weiner S, Traub W. Organization of hydroxyapatite crystals within collagen fibrils. FEBS Lett. 1986;206:262-6.
12. Alexander B, Daulton TL, Genin GM, Lipner J, Pasteris JD, Wopenka B, et al. The nanometre-scale physiology of bone: steric modelling and scanning transmission electron microscopy of collagen–mineral structure. J R Soc Interface. 2012;9:1774-86.
13. Reznikov N, Shahar R, Weiner S. Three-dimensional structure of human lamellar bone: the presence of two different materials and new insights into the hierarchical organization. Bone. 2014;59:93-104.
14. Mahamid J, Aichmayer B, Shimoni E, Ziblat R, Li C, Siegel S, et al. Mapping amorphous calcium phosphate transformation into crystalline mineral from the cell to the bone in zebrafish fin rays. Proc Natl Acad Sci U S A. 2010;107:6316-21.
15. Mann S, Webb J, Williams RJP. Biomineralization: chemical and biochemical perspectives. Weinheim: VCH; 1989.

16. Olszta MJ, Cheng X, Jee SS, Kumar R, Kim Y-Y, Kaufman MJ, et al. Bone structure and formation: A new perspective. Mater Sci Eng R Rep. 2007;58:77-116.
17. McNally EA, Schwarcz HP, Botton GA, Arsenault AL. A model for the ultrastructure of bone based on electron microscopy of ion-milled sections. PLoS One. 2012;7:e29258.
18. McNally E, Nan F, Botton GA, Schwarcz HP. Scanning transmission electron microscopic tomography of cortical bone using Z-contrast imaging. Micron. 2013;49:46-53.
19. Schwarcz HP, McNally EA, Botton GA. Dark-field transmission electron microscopy of cortical bone reveals details of extrafibrillar crystals. J Struct Biol. 2014;188:240-8.
20. Jantou V, Turmaine M, West GD, Horton MA, McComb DW. Focused ion beam milling and ultramicrotomy of mineralised ivory dentine for analytical transmission electron microscopy. Micron. 2009;40:495-501.
21. Jantou-Morris V, Horton MA, McComb DW. The nano-morphological relationships between apatite crystals and collagen fibrils in ivory dentine. Biomaterials. 2010;31:5275-86.
22. Pazzaglia UE, Congiu T, Marchese M, Dell'Orbo C. The shape modulation of osteoblast-osteocyte transformation and its correlation with the fibrillar organization in secondary osteons: a SEM study employing the graded osmic maceration technique. Cell Tissue Res. 2010;340:533-40.
23. Yerramshetty JS, Akkus O. The associations between mineral crystallinity and the mechanical properties of human cortical bone. Bone. 2008;42:476-82.
24. Currey JD, Brear K, Zioupos P. The effects of ageing and changes in mineral content in degrading the toughness of human femora. J Biomech. 1996;29:257-60.
25. Burr DB. The contribution of the organic matrix to bone's material properties. Bone. 2002;31:8-11.
26. Legeros RZ, Trautz OR, Legeros JP, Klein E, Shirra WP. Apatite crystallites: effects of carbonate on morphology. Science. 1967;155:1409-11.
27. Busa B, Miller LM, Rubin CT, Qin YX, Judex S. Rapid establishment of chemical and mechanical properties during lamellar bone formation. Calcif Tissue Int. 2005;77:386-94.
28. Awonusi A, Morris MD, Tecklenburg MM. Carbonate assignment and calibration in the Raman spectrum of apatite. Calcif Tissue Int. 2007;81:46-52.
29. Yerramshetty JS, Lind C, Akkus O. The compositional and physicochemical homogeneity of male femoral cortex increases after the sixth decade. Bone. 2006;39:1236-43.
30. Wopenka B, Pasteris JD. A mineralogical perspective on the apatite in bone. Mater Sci Eng C Mater Biol Appl. 2005;25:131-43.

31. Taylor MG, Parker SF, Simkiss K, Mitchell PCH. Bone mineral: evidence for hydroxy groups by inelastic neutron scattering. Phys Chem Chem Phys. 2001;3:1514-7.
32. Pasteris JD, Wopenka B, Freeman JJ, Rogers K, Valsami-Jones E, van der Houwen JAM, et al. Lack of OH in nanocrystalline apatite as a function of degree of atomic order: implications for bone and biomaterials. Biomaterials. 2004;25:229-38.
33. Müller R. Hierarchical microimaging of bone structure and function. Nat Rev Rheumatol. 2009;5:373-81.
34. Georgiadis M, Müller R, Schneider P. Techniques to assess bone ultrastructure organization: orientation and arrangement of mineralized collagen fibrils. J R Soc Interface. 2016;13.
35. Bayliss L, Mahoney DJ, Monk P. Normal bone physiology, remodelling and its hormonal regulation. Surgery. 2012;30:47-53.
36. Crockett JC, Rogers MJ, Coxon FP, Hocking LJ, Helfrich MH. Bone remodelling at a glance. J Cell Sci. 2011;124:991.
37. Schaffler MB, Cheung WY, Majeska R, Kennedy O. Osteocytes: master orchestrators of bone. Calcif Tissue Int. 2014;94:5-24.
38. Bellido T. Osteocyte-driven bone remodeling. Calcif Tissue Int. 2014;94:25-34.
39. Robling AG, Niziolek PJ, Baldridge LA, Condon KW, Allen MR, Alam I, et al. Mechanical stimulation of bone in vivo reduces osteocyte expression of Sost/sclerostin. J Biol Chem. 2008;283:5866-75.
40. Nakashima T, Hayashi M, Fukunaga T, Kurata K, Oh-Hora M, Feng JQ, et al. Evidence for osteocyte regulation of bone homeostasis through RANKL expression. Nat Med. 2011;17:1231-4.
41. Buenzli PR, Sims NA. Quantifying the osteocyte network in the human skeleton. Bone. 2015;75:144-50.
42. Bonewald LF. The amazing osteocyte. J Bone Miner Res. 2011;26:229-38.
43. Bonewald LF. Generation and function of osteocyte dendritic processes. J Musculoskelet Neuronal Interact. 2005;5:321-4.
44. Palumbo C, Ferretti M, Marotti G. Osteocyte dendrogenesis in static and dynamic bone formation: an ultrastructural study. Anat Rec A Discov Mol Cell Evol Biol. 2004;278:474-80.
45. Franz-Odendaal TA, Hall BK, Witten PE. Buried alive: how osteoblasts become osteocytes. Dev Dyn. 2006;235:176-90.
46. Pazzaglia UE, Congiu T, Sibilia V, Quacci D. Osteoblast-osteocyte transformation. A SEM densitometric analysis of endosteal apposition in rabbit femur. J Anat. 2014;224:132-41.
47. Dallas SL, Bonewald LF. Dynamics of the Transition from Osteoblast to Osteocyte. Ann N Y Acad Sci. 2010;1192:437-43.
48. Jones SJ, Boyde A, Pawley JB. Osteoblasts and collagen orientation. Cell Tissue Res. 1975;159:73-80.

49. Han Y, Cowin SC, Schaffler MB, Weinbaum S. Mechanotransduction and strain amplification in osteocyte cell processes. Proc Natl Acad Sci U S A. 2004;101:16689-94.
50. Burra S, Nicolella DP, Francis WL, Freitas CJ, Mueschke NJ, Poole K, et al. Dendritic processes of osteocytes are mechanotransducers that induce the opening of hemichannels. Proc Natl Acad Sci U S A. 2010;107:13648-53.
51. Thi MM, Suadicani SO, Schaffler MB, Weinbaum S, Spray DC. Mechanosensory responses of osteocytes to physiological forces occur along processes and not cell body and require α(V)β(3) integrin. Proc Natl Acad Sci U S A. 2013;110:21012-7.
52. You L, Temiyasathit S, Lee P, Kim CH, Tummala P, Yao W, et al. Osteocytes as mechanosensors in the inhibition of bone resorption due to mechanical loading. Bone. 2008;42:172-9.
53. Klein-Nulend J, Bakker AD, Bacabac RG, Vatsa A, Weinbaum S. Mechanosensation and transduction in osteocytes. Bone. 2013;54:182-90.
54. Frost HM. Micropetrosis. J Bone Joint Surg Am. 1960;42-A:144-50.
55. Boyde A. The real response of bone to exercise. J Anat. 2003;203:173-89.
56. Carpentier VT, Wong J, Yeap Y, Gan C, Sutton-Smith P, Badiei A, et al. Increased proportion of hypermineralized osteocyte lacunae in osteoporotic and osteoarthritic human trabecular bone: implications for bone remodeling. Bone. 2012;50:688-94.
57. Milovanovic P, Zimmermann EA, vom Scheidt A, Hoffmann B, Sarau G, Yorgan T, et al. The Formation of Calcified Nanospherites during Micropetrosis Represents a Unique Mineralization Mechanism in Aged Human Bone. Small. 2017;13:1602215.
58. Jilka RL, Noble B, Weinstein RS. Osteocyte apoptosis. Bone. 2013;54:264-71.
59. Busse B, Djonic D, Milovanovic P, Hahn M, Puschel K, Ritchie RO, et al. Decrease in the osteocyte lacunar density accompanied by hypermineralized lacunar occlusion reveals failure and delay of remodeling in aged human bone. Aging Cell. 2010;9:1065-75.
60. Vashishth D, Verborgt O, Divine G, Schaffler MB, Fyhrie DP. Decline in osteocyte lacunar density in human cortical bone is associated with accumulation of microcracks with age. Bone. 2000;26:375-80.
61. Vashishth D, Gibson G, Kimura J, Schaffler MB, Fyhrie DP. Determination of bone volume by osteocyte population. Anat Rec. 2002;267:292-5.
62. Hunter RL, Agnew AM. Intraskeletal variation in human cortical osteocyte lacunar density: Implications for bone quality assessment. Bone Rep. 2016;5:252-61.

63. Yeni YN, Vashishth D, Fyhrie DP. Estimation of bone matrix apparent stiffness variation caused by osteocyte lacunar size and density. J Biomech Eng. 2001;123:10-7.
64. Atkins A, Dean MN, Habegger ML, Motta PJ, Ofer L, Repp F, et al. Remodeling in bone without osteocytes: billfish challenge bone structure-function paradigms. Proc Natl Acad Sci U S A. 2014;111:16047-52.
65. Atkins A, Reznikov N, Ofer L, Masic A, Weiner S, Shahar R. The three-dimensional structure of anosteocytic lamellated bone of fish. Acta Biomater. 2015;13:311-23.
66. Atkins A, Milgram J, Weiner S, Shahar R. The response of anosteocytic bone to controlled loading. J Exp Biol. 2015;218:3559-69.
67. Kerschnitzki M, Wagermaier W, Roschger P, Seto J, Shahar R, Duda GN, et al. The organization of the osteocyte network mirrors the extracellular matrix orientation in bone. J Struct Biol. 2011;173:303-11.
68. Kerschnitzki M, Kollmannsberger P, Burghammer M, Duda GN, Weinkamer R, Wagermaier W, et al. Architecture of the osteocyte network correlates with bone material quality. J Bone Miner Res. 2013;28:1837-45.
69. Repp F, Kollmannsberger P, Roschger A, Kerschnitzki M, Berzlanovich A, Gruber GM, et al. Spatial heterogeneity in the canalicular density of the osteocyte network in human osteons. Bone Rep. 2017;6:101-8.
70. Liu Y, Manjubala I, Schell H, Epari DR, Roschger P, Duda GN, et al. Size and habit of mineral particles in bone and mineralized callus during bone healing in sheep. J Bone Miner Res. 2010;25:2029-38.
71. Jones SJ. Secretory territories and rate of matrix production of osteoblasts. Calcif Tissue Res. 1974;14:309-15.
72. Lin Y, Xu S. AFM analysis of the lacunar-canalicular network in demineralized compact bone. J Microsc. 2011;241:291-302.
73. Sugawara Y, Kamioka H, Honjo T, Tezuka K, Takano-Yamamoto T. Three-dimensional reconstruction of chick calvarial osteocytes and their cell processes using confocal microscopy. Bone. 2005;36:877-83.
74. Shapiro F. Bone development and its relation to fracture repair. The role of mesenchymal osteoblasts and surface osteoblasts. Eur Cell Mater. 2008;15:53-76.
75. Brånemark PI, Hansson BO, Adell R, Breine U, Lindström J, Hallen O, et al. Osseointegrated implants in the treatment of the edentulous jaw. Experience from a 10-year period. Scand J Plast Reconstr Surg Suppl. 1977;16:1-132.
76. Janko M, Zink A, Gigler AM, Heckl WM, Stark RW. Nanostructure and mechanics of mummified type I collagen from the 5300-year-old Tyrolean Iceman. Proc Biol Sci. 2010;277:2301-9.
77. Bertazzo S, Maidment SC, Kallepitis C, Fearn S, Stevens MM, Xie HN. Fibres and cellular structures preserved in 75-million-year-old dinosaur specimens. Nat Commun. 2015;6:7352.

78. Albrektsson T, Brånemark PI, Hansson HA, Lindström J. Osseointegrated titanium implants. Requirements for ensuring a long-lasting, direct bone-to-implant anchorage in man. Acta Orthop Scand. 1981;52:155-70.
79. Trindade R, Albrektsson T, Tengvall P, Wennerberg A. Foreign Body Reaction to Biomaterials: On Mechanisms for Buildup and Breakdown of Osseointegration. Clin Implant Dent Relat Res. 2016;18:192-203.
80. Davies JE. Understanding peri-implant endosseous healing. J Dent Educ. 2003;67:932-49.
81. Franchi M, Bacchelli B, Martini D, Pasquale VD, Orsini E, Ottani V, et al. Early detachment of titanium particles from various different surfaces of endosseous dental implants. Biomaterials. 2004;25:2239-46.
82. Franchi M, Fini M, Martini D, Orsini E, Leonardi L, Ruggeri A, et al. Biological fixation of endosseous implants. Micron. 2005;36:665-71.
83. Albrektsson T, Brånemark PI, Hansson H-A, Kasemo B, Larsson K, Lundström I, et al. The interface zone of inorganic implants in vivo: Titanium implants in bone. Ann Biomed Eng. 1983;11:1-27.
84. Lindahl C, Borchardt P, Lausmaa J, Xia W, Engqvist H. Studies of early growth mechanisms of hydroxyapatite on single crystalline rutile: a model system for bioactive surfaces. J Mater Sci Mater Med. 2010;21:2743-9.
85. Lindberg F, Heinrichs J, Ericson F, Thomsen P, Engqvist H. Hydroxylapatite growth on single-crystal rutile substrates. Biomaterials. 2008;29:3317-23.
86. Wennerberg A, Albrektsson T. Effects of titanium surface topography on bone integration: a systematic review. Clin Oral Implants Res. 2009;20 Suppl 4:172-84.
87. Shah FA, Trobos M, Thomsen P, Palmquist A. Commercially pure titanium (cp-Ti) versus titanium alloy (Ti6Al4V) materials as bone anchored implants — Is one truly better than the other? Mater Sci Eng C Mater Biol Appl. 2016;62:960-6.
88. Cordeiro JM, Barão VAR. Is there scientific evidence favoring the substitution of commercially pure titanium with titanium alloys for the manufacture of dental implants? Mater Sci Eng C Mater Biol Appl. 2017;71:1201-15.
89. Thomsen P, Larsson C, Ericson LE, Sennerby L, Lausmaa J, Kasemo B. Structure of the interface between rabbit cortical bone and implants of gold, zirconium and titanium. J Mater Sci Mater Med. 1997;8:653-65.
90. Stevenson A. Oxford Dictionary of English: OUP Oxford; 2010.
91. Luklinska ZB, Bonfield W. Morphology and ultrastructure of the interface between hydroxyapatite-polyhydroxybutyrate composite implant and bone. J Mater Sci Mater Med. 1997;8:379-83.

92. Donath K, Breuner G. A method for the study of undecalcified bones and teeth with attached soft tissues. The Sage-Schliff (sawing and grinding) technique. J Oral Pathol. 1982;11:318-26.
93. Albrektsson T, Hansson HA, Ivarsson B. Interface analysis of titanium and zirconium bone implants. Biomaterials. 1985;6:97-101.
94. Linder L, Albrektsson T, Brånemark PI, Hansson HA, Ivarsson B, Jonsson U, et al. Electron microscopic analysis of the bone-titanium interface. Acta Orthop Scand. 1983;54:45-52.
95. Thomsen P, Ericson LE. Light and transmission electron microscopy used to study the tissue morphology close to implants. Biomaterials. 1985;6:421-4.
96. Steflik DE, Hanes PJ, Sisk AL, Parr GR, Song MJ, Lake FT, et al. Transmission electron microscopic and high voltage electron microscopic observations of the bone and osteocyte activity adjacent to unloaded dental implants placed in dogs. J Periodontol. 1992;63:443-52.
97. Steflik DE, Sisk AL, Parr GR, Lake FT, Hanes PJ, Berkery DJ, et al. Transmission electron and high-voltage electron microscopy of osteocyte cellular processes extending to the dental implant surface. J Biomed Mater Res. 1994;28:1095-107.
98. Steflik DE, Corpe RS, Lake FT, Young TR, Sisk AL, Parr GR, et al. Ultrastructural analyses of the attachment (bonding) zone between bone and implanted biomaterials. J Biomed Mater Res. 1998;39:611-20.
99. Sennerby L, Thomsen P, Ericson LE. Early tissue response to titanium implants inserted in rabbit cortical bone. J Mater Sci Mater Med. 1993;4:494-502.
100. Davies JE. Bone bonding at natural and biomaterial surfaces. Biomaterials. 2007;28:5058-67.
101. Davies JE, Ajami E, Moineddin R, Mendes VC. The roles of different scale ranges of surface implant topography on the stability of the bone/implant interface. Biomaterials. 2013;34:3535-46.
102. Davies JE, Mendes VC, Ko JC, Ajami E. Topographic scale-range synergy at the functional bone/implant interface. Biomaterials. 2014;35:25-35.
103. Chen P-Y, Toroian D, Price PA, McKittrick J. Minerals Form a Continuum Phase in Mature Cancellous Bone. Calcif Tissue Int. 2011;88:351-61.
104. Tertuliano OA, Greer JR. The nanocomposite nature of bone drives its strength and damage resistance. Nat Mater. 2016;15:1195-202.
105. Burr DB, Schaffler MB, Frederickson RG. Composition of the cement line and its possible mechanical role as a local interface in human compact bone. J Biomech. 1988;21:939-45.
106. Skedros JG, Holmes JL, Vajda EG, Bloebaum RD. Cement lines of secondary osteons in human bone are not mineral-deficient: New data in a historical perspective. Anat Rec A Discov Mol Cell Evol Biol. 2005;286A:781-803.

107. Mckee MD, Nanci A. Osteopontin: An Interfacial Extracellular Matrix Protein in Mineralized Tissues. Connect Tissue Res. 1996;35:197-205.
108. Puleo DA, Nanci A. Understanding and controlling the bone–implant interface. Biomaterials. 1999;20:2311-21.
109. Ayukawa Y, Takeshita F, Inoue T, Yoshinari M, Shimono M, Suetsugu T, et al. An immunoelectron microscopic localization of noncollagenous bone proteins (osteocalcin and osteopontin) at the bone-titanium interface of rat tibiae. J Biomed Mater Res. 1998;41:111-9.
110. Giannuzzi LA, Phifer D, Giannuzzi NJ, Capuano MJ. Two-Dimensional and 3-Dimensional Analysis of Bone/Dental Implant Interfaces With the Use of Focused Ion Beam and Electron Microscopy. J Oral Maxillofac Surg. 2007;65:737-47.
111. Palmquist A, Jarmar T, Emanuelsson L, Brånemark R, Engqvist H, Thomsen P. Forearm bone-anchored amputation prosthesis: a case study on the osseointegration. Acta Orthop. 2008;79:78-85.
112. Liu X, Chu PK, Ding C. Surface modification of titanium, titanium alloys, and related materials for biomedical applications. Mater Sci Eng R Rep. 2004;47:49-121.
113. Le Guéhennec L, Soueidan A, Layrolle P, Amouriq Y. Surface treatments of titanium dental implants for rapid osseointegration. Dent Mater. 2007;23:844-54.
114. Lennerås M, Palmquist A, Norlindh B, Emanuelsson L, Thomsen P, Omar O. Oxidized Titanium Implants Enhance Osseointegration via Mechanisms Involving RANK/RANKL/OPG Regulation. Clin Implant Dent Relat Res. 2015;17 Suppl 2:e486-500.
115. Dohan Ehrenfest DM, Coelho PG, Kang B-S, Sul Y-T, Albrektsson T. Classification of osseointegrated implant surfaces: materials, chemistry and topography. Trends Biotechnol. 2010;28:198-206.
116. Mendonça G, Mendonça DBS, Aragão FJL, Cooper LF. Advancing dental implant surface technology – From micron- to nanotopography. Biomaterials. 2008;29:3822-35.
117. Bjursten LM, Rasmusson L, Oh S, Smith GC, Brammer KS, Jin S. Titanium dioxide nanotubes enhance bone bonding in vivo. J Biomed Mater Res A. 2010;92:1218-24.
118. Park J, Bauer S, Schlegel KA, Neukam FW, von der Mark K, Schmuki P. TiO2 nanotube surfaces: 15 nm--an optimal length scale of surface topography for cell adhesion and differentiation. Small. 2009;5:666-71.
119. Park J, Bauer S, von der Mark K, Schmuki P. Nanosize and vitality: TiO2 nanotube diameter directs cell fate. Nano Lett. 2007;7:1686-91.
120. Variola F, Brunski JB, Orsini G, Tambasco de Oliveira P, Wazen R, Nanci A. Nanoscale surface modifications of medically relevant metals: state-of-the art and perspectives. Nanoscale. 2011;3:335-53.

121. Variola F, Vetrone F, Richert L, Jedrzejowski P, Yi JH, Zalzal S, et al. Improving biocompatibility of implantable metals by nanoscale modification of surfaces: an overview of strategies, fabrication methods, and challenges. Small. 2009;5:996-1006.
122. Vetrone F, Variola F, Tambasco de Oliveira P, Zalzal SF, Yi JH, Sam J, et al. Nanoscale oxidative patterning of metallic surfaces to modulate cell activity and fate. Nano Lett. 2009;9:659-65.
123. Kurella A, Dahotre NB. Review paper: surface modification for bioimplants: the role of laser surface engineering. J Biomater Appl. 2005;20:5-50.
124. Chichkov BN, Momma C, Nolte S, von Alvensleben F, Tünnermann A. Femtosecond, picosecond and nanosecond laser ablation of solids. Appl Phys A. 1996;63:109-15.
125. Nolte S, Momma C, Jacobs H, Tünnermann A, Chichkov BN, Wellegehausen B, et al. Ablation of metals by ultrashort laser pulses. J Opt Soc Am B. 1997;14:2716-22.
126. Kamlage G, Bauer T, Ostendorf A, Chichkov BN. Deep drilling of metals by femtosecond laser pulses. Appl Phys A. 2003;77:307-10.
127. Gaggl A, Schultes G, Müller WD, Kärcher H. Scanning electron microscopical analysis of laser-treated titanium implant surfaces--a comparative study. Biomaterials. 2000;21:1067-73.
128. Trtica M, Gakovic B, Batani D, Desai T, Panjan P, Radak B. Surface modifications of a titanium implant by a picosecond Nd:YAG laser operating at 1064 and 532 nm. Appl Surf Sci. 2006;253:2551-6.
129. Brånemark R, Emanuelsson L, Palmquist A, Thomsen P. Bone response to laser-induced micro- and nano-size titanium surface features. Nanomedicine. 2011;7:220-7.
130. Murr LE, Gaytan SM, Medina F, Lopez H, Martinez E, Machado BI, et al. Next-generation biomedical implants using additive manufacturing of complex, cellular and functional mesh arrays. Philos Trans A Math Phys Eng Sci. 2010;368:1999-2032.
131. Amin Yavari S, Ahmadi SM, Wauthle R, Pouran B, Schrooten J, Weinans H, et al. Relationship between unit cell type and porosity and the fatigue behavior of selective laser melted meta-biomaterials. J Mech Behav Biomed Mater. 2015;43:91-100.
132. Derand P, Rannar LE, Hirsch JM. Imaging, virtual planning, design, and production of patient-specific implants and clinical validation in craniomaxillofacial surgery. Craniomaxillofac Trauma Reconstr. 2012;5:137-44.
133. Suska F, Kjeller G, Tarnow P, Hryha E, Nyborg L, Snis A, et al. Electron Beam Melting Manufacturing Technology for Individually Manufactured Jaw Prosthesis: A Case Report. J Oral Maxillofac Surg. 2016;74:1706.e1-.e15.

134. Murr LE, Amato KN, Li SJ, Tian YX, Cheng XY, Gaytan SM, et al. Microstructure and mechanical properties of open-cellular biomaterials prototypes for total knee replacement implants fabricated by electron beam melting. J Mech Behav Biomed Mater. 2011;4:1396-411.
135. Ryan G, Pandit A, Apatsidis DP. Fabrication methods of porous metals for use in orthopaedic applications. Biomaterials. 2006;27:2651-70.
136. Navarro M, Michiardi A, Castano O, Planell JA. Biomaterials in orthopaedics. J R Soc Interface. 2008;5:1137-58.
137. Huiskes R, Weinans H, van Rietbergen B. The relationship between stress shielding and bone resorption around total hip stems and the effects of flexible materials. Clin Orthop Relat Res. 1992:124-34.
138. Heinl P, Müller L, Körner C, Singer RF, Müller FA. Cellular Ti–6Al–4V structures with interconnected macro porosity for bone implants fabricated by selective electron beam melting. Acta Biomater. 2008;4:1536-44.
139. Thomsen P, Malmström J, Emanuelsson L, Rene M, Snis A. Electron beam-melted, free-form-fabricated titanium alloy implants: Material surface characterization and early bone response in rabbits. J Biomed Mater Res B Appl Biomater. 2009;90B:35-44.
140. Palmquist A, Snis A, Emanuelsson L, Browne M, Thomsen P. Long-term biocompatibility and osseointegration of electron beam melted, free-form-fabricated solid and porous titanium alloy: experimental studies in sheep. J Biomater Appl. 2013;27:1003-16.
141. Tkachenko S, Datskevich O, Kulak L, Jacobson S, Engqvist H, Persson C. Wear and friction properties of experimental Ti-Si-Zr alloys for biomedical applications. J Mech Behav Biomed Mater. 2014;39:61-72.
142. Saldivar-Garcia AJ, Lopez HF. Microstructural effects on the wear resistance of wrought and as-cast Co-Cr-Mo-C implant alloys. J Biomed Mater Res A. 2005;74:269-74.
143. Chiba A, Kumagai K, Nomura N, Miyakawa S. Pin-on-disk wear behavior in a like-on-like configuration in a biological environment of high carbon cast and low carbon forged Co-29Cr-6Mo alloys. Acta Materialia. 2007;55:1309-18.
144. Sotereanos NG, Engh CA, Glassman AH, Macalino GE, Engh CA, Jr. Cementless femoral components should be made from cobalt chrome. Clin Orthop Relat Res. 1995:146-53.
145. Engh CA, Bobyn JD, Glassman AH. Porous-coated hip replacement. The factors governing bone ingrowth, stress shielding, and clinical results. J Bone Joint Surg Br. 1987;69:45-55.
146. Sychterz CJ, Engh CA. The influence of clinical factors on periprosthetic bone remodeling. Clin Orthop Relat Res. 1996:285-92.
147. Bobyn JD, Glassman AH, Goto H, Krygier JJ, Miller JE, Brooks CE. The effect of stem stiffness on femoral bone resorption after

canine porous-coated total hip arthroplasty. Clin Orthop Relat Res. 1990:196-213.
148. Jinno T, Goldberg VM, Davy D, Stevenson S. Osseointegration of surface-blasted implants made of titanium alloy and cobalt-chromium alloy in a rabbit intramedullary model. J Biomed Mater Res. 1998;42:20-9.
149. Jakobsen SS, Baas J, Jakobsen T, Soballe K. Biomechanical implant fixation of CoCrMo coating inferior to titanium coating in a canine implant model. J Biomed Mater Res A. 2010;94:180-6.
150. Palmquist A, Jarmar T, Hermansson L, Emanuelsson L, Taylor A, Taylor M, et al. Calcium aluminate coated and uncoated free form fabricated CoCr implants: a comparative study in rabbit. J Biomed Mater Res B Appl Biomater. 2009;91B:122-7.
151. Grandfield K, Palmquist A, Goncalves S, Taylor A, Taylor M, Emanuelsson L, et al. Free form fabricated features on CoCr implants with and without hydroxyapatite coating in vivo: a comparative study of bone contact and bone growth induction. J Mater Sci Mater Med. 2011;22:899-906.
152. Linder L. Osseointegration of metallic implants. I. Light microscopy in the rabbit. Acta Orthop Scand. 1989;60:129-34.
153. Linder L, Obrant K, Boivin G. Osseointegration of metallic implants. II. Transmission electron microscopy in the rabbit. Acta Orthop Scand. 1989;60:135-9.
154. Stenlund P, Kurosu S, Koizumi Y, Suska F, Matsumoto H, Chiba A, et al. Osseointegration Enhancement by Zr doping of Co-Cr-Mo Implants Fabricated by Electron Beam Melting. Additive Manufacturing. 2015;6:6-15.
155. Stangl R, Pries A, Loos B, Müller M, Erben RG. Influence of pores created by laser superfinishing on osseointegration of titanium alloy implants. J Biomed Mater Res A. 2004;69:444-53.
156. Götz HE, Müller M, Emmel A, Holzwarth U, Erben RG, Stangl R. Effect of surface finish on the osseointegration of laser-treated titanium alloy implants. Biomaterials. 2004;25:4057-64.
157. Aido M, Kerschnitzki M, Hoerth R, Burghammer M, Montero C, Checa S, et al. Relationship between nanoscale mineral properties and calcein labeling in mineralizing bone surfaces. Connect Tissue Res. 2014;55 Suppl 1:15-7.
158. Shah FA, Zanghellini E, Matic A, Thomsen P, Palmquist A. The Orientation of Nanoscale Apatite Platelets in Relation to Osteoblastic-Osteocyte Lacunae on Trabecular Bone Surface. Calcif Tissue Int. 2016;98:193-205.
159. Shah FA, Palmquist A. Evidence that Osteocytes in Autogenous Bone Fragments can Repair Disrupted Canalicular Networks and Connect with Osteocytes in de novo Formed Bone on the Fragment Surface. Calcif Tissue Int. 2017;101:1-7.

160. Shah FA, Johansson ML, Omar O, Simonsson H, Palmquist A, Thomsen P. Laser-Modified Surface Enhances Osseointegration and Biomechanical Anchorage of Commercially Pure Titanium Implants for Bone-Anchored Hearing Systems. PLoS One. 2016;11:e0157504.
161. Shah FA, Nilson B, Brånemark R, Thomsen P, Palmquist A. The bone-implant interface – nanoscale analysis of clinically retrieved dental implants. Nanomedicine. 2014;10:1729-37.
162. Shah FA, Wang X, Thomsen P, Grandfield K, Palmquist A. High-Resolution Visualization of the Osteocyte Lacuno-Canalicular Network Juxtaposed to the Surface of Nanotextured Titanium Implants in Human. ACS Biomater Sci Eng. 2015;1:305-13.
163. Shah FA, Snis A, Matic A, Thomsen P, Palmquist A. 3D printed Ti6Al4V implant surface promotes bone maturation and retains a higher density of less aged osteocytes at the bone-implant interface. Acta Biomater. 2016;30:357-67.
164. Shah FA, Omar O, Suska F, Snis A, Matic A, Emanuelsson L, et al. Long-term osseointegration of 3D printed CoCr constructs with an interconnected open-pore architecture prepared by electron beam melting. Acta Biomater. 2016;36:296-309.
165. Grandfield K, McNally EA, Palmquist A, Botton GA, Thomsen P, Engqvist H. Visualizing biointerfaces in three dimensions: electron tomography of the bone–hydroxyapatite interface. J R Soc Interface. 2010;7:1497-501.
166. Wang X, Shah FA, Palmquist A, Grandfield K. 3D characterization of human nano-osseointegration by on-axis electron tomography without the missing wedge. ACS Biomater Sci Eng. 2016;3:49-55.
167. Grandfield K, Palmquist A, Engqvist H. Three-dimensional structure of laser-modified Ti6Al4V and bone interface revealed with STEM tomography. Ultramicroscopy. 2013;127:48-52.
168. Oliver WC, Pharr GM. An improved technique for determining hardness and elastic modulus using load and displacement sensing indentation experiments. J Mater Res. 2011;7:1564-83.
169. Ebenstein DM, Pruitt LA. Nanoindentation of biological materials. Nano Today. 2006;1:26-33.
170. Rezakhaniha R, Agianniotis A, Schrauwen JTC, Griffa A, Sage D, Bouten CVC, et al. Experimental investigation of collagen waviness and orientation in the arterial adventitia using confocal laser scanning microscopy. Biomech Model Mechanobiol. 2012;11:461-73.
171. Vatsa A, Breuls RG, Semeins CM, Salmon PL, Smit TH, Klein-Nulend J. Osteocyte morphology in fibula and calvaria — Is there a role for mechanosensing? Bone. 2008;43:452-8.
172. Dong P, Haupert S, Hesse B, Langer M, Gouttenoire P-J, Bousson V, et al. 3D osteocyte lacunar morphometric properties and

distributions in human femoral cortical bone using synchrotron radiation micro-CT images. Bone. 2014;60:172-85.
173. Bell LS, Kayser M, Jones C. The mineralized osteocyte: A living fossil. American Journal of Physical Anthropology. 2008;137:449-56.
174. Lieberman JR, Daluiski A, Einhorn TA. The role of growth factors in the repair of bone. Biology and clinical applications. J Bone Joint Surg Am. 2002;84-a:1032-44.
175. Miron RJ, Gruber R, Hedbom E, Saulacic N, Zhang Y, Sculean A, et al. Impact of bone harvesting techniques on cell viability and the release of growth factors of autografts. Clin Implant Dent Relat Res. 2013;15:481-9.
176. Sasaki M, Kuroshima S, Aoki Y, Inaba N, Sawase T. Ultrastructural alterations of osteocyte morphology via loaded implants in rabbit tibiae. J Biomech. 2015;48:4130-41.
177. Shah FA, Johansson BR, Thomsen P, Palmquist A. Ultrastructural evaluation of shrinkage artefacts induced by fixatives and embedding resins on osteocyte processes and pericellular space dimensions. J Biomed Mater Res A. 2015;103:1565-76.
178. Mohammadi S, Esposito M, Hall J, Emanuelsson L, Krozer A, Thomsen P. Long-term bone response to titanium implants coated with thin radiofrequent magnetron-sputtered hydroxyapatite in rabbits. Int J Oral Maxillofac Implants. 2004;19:498-509.
179. Mohammadi S, Esposito M, Hall J, Emanuelsson L, Krozer A, Thomsen P. Short-term bone response to titanium implants coated with thin radiofrequent magnetron-sputtered hydroxyapatite in rabbits. Clin Implant Dent Relat Res. 2003;5:241-53.
180. Palmquist A, Emanuelsson L, Brånemark R, Thomsen P. Biomechanical, histological and ultrastructural analyses of laser micro- and nano-structured titanium implant after 6 months in rabbit. J Biomed Mater Res B Appl Biomater. 2011;97:289-98.
181. Palmquist A, Lindberg F, Emanuelsson L, Brånemark R, Engqvist H, Thomsen P. Biomechanical, histological, and ultrastructural analyses of laser micro- and nano-structured titanium alloy implants: a study in rabbit. J Biomed Mater Res A. 2010;92:1476-86.
182. Shah FA, Stenlund P, Martinelli A, Thomsen P, Palmquist A. Direct communication between osteocytes and acid-etched titanium implants with a sub-micron topography. J Mater Sci Mater Med. 2016;27:167.
183. Sennerby L, Ericson LE, Thomsen P, Lekholm U, Astrand P. Structure of the bone-titanium interface in retrieved clinical oral implants. Clin Oral Implants Res. 1991;2:103-11.
184. Milovanovic P, Zimmermann EA, Hahn M, Djonic D, Püschel K, Djuric M, et al. Osteocytic Canalicular Networks: Morphological Implications for Altered Mechanosensitivity. ACS Nano. 2013;7:7542-51.

185. You LD, Weinbaum S, Cowin SC, Schaffler MB. Ultrastructure of the osteocyte process and its pericellular matrix. Anat Rec A Discov Mol Cell Evol Biol. 2004;278:505-13.
186. McNamara LM, Majeska RJ, Weinbaum S, Friedrich V, Schaffler MB. Attachment of osteocyte cell processes to the bone matrix. Anat Rec (Hoboken). 2009;292:355-63.
187. You L, Cowin SC, Schaffler MB, Weinbaum S. A model for strain amplification in the actin cytoskeleton of osteocytes due to fluid drag on pericellular matrix. J Biomech. 2001;34:1375-86.
188. Lau E, Al-Dujaili S, Guenther A, Liu D, Wang L, You L. Effect of low-magnitude, high-frequency vibration on osteocytes in the regulation of osteoclasts. Bone. 2010;46:1508-15.
189. Mann V, Huber C, Kogianni G, Jones D, Noble B. The influence of mechanical stimulation on osteocyte apoptosis and bone viability in human trabecular bone. J Musculoskelet Neuronal Interact. 2006;6:408-17.
190. Palmquist A, Grandfield K, Norlindh B, Mattsson T, Brånemark R, Thomsen P. Bone-titanium oxide interface in humans revealed by transmission electron microscopy and electron tomography. J R Soc Interface. 2012;9:396-400.
191. Palmquist A, Emanuelsson L, Sjövall P. Chemical and structural analysis of the bone-implant interface by TOF-SIMS, SEM, FIB and TEM: Experimental study in animal. Appl Surf Sci. 2012;258:6485-94.
192. Grandfield K, Gustafsson S, Palmquist A. Where bone meets implant: the characterization of nano-osseointegration. Nanoscale. 2013;5:4302-8.
193. Genin GM, Kent A, Birman V, Wopenka B, Pasteris JD, Marquez PJ, et al. Functional grading of mineral and collagen in the attachment of tendon to bone. Biophys J. 2009;97:976-85.
194. Hang F, Gupta HS, Barber AH. Nanointerfacial strength between non-collagenous protein and collagen fibrils in antler bone. J R Soc Interface. 2014;11:20130993.
195. Huiskes R. The various stress patterns of press-fit, ingrown, and cemented femoral stems. Clin Orthop Relat Res. 1990:27-38.
196. Turner CH, Rho J, Takano Y, Tsui TY, Pharr GM. The elastic properties of trabecular and cortical bone tissues are similar: results from two microscopic measurement techniques. J Biomech. 1999;32:437-41.
197. Amin Yavari S, van der Stok J, Chai YC, Wauthle R, Tahmasebi Birgani Z, Habibovic P, et al. Bone regeneration performance of surface-treated porous titanium. Biomaterials. 2014;35:6172-81.
198. Sugiyama T, Price JS, Lanyon LE. Functional adaptation to mechanical loading in both cortical and cancellous bone is controlled locally and is confined to the loaded bones. Bone. 2010;46:314-21.
199. Christen P, Ito K, Ellouz R, Boutroy S, Sornay-Rendu E, Chapurlat RD, et al. Bone remodelling in humans is load-driven but not lazy. Nat Commun. 2014;5:4855.

200. Gibson LJ, Ashby MF. Cellular Solids: Structure and Properties: Cambridge University Press; 1999.
201. Geng H, Todd NM, Devlin-Mullin A, Poologasundarampillai G, Kim TB, Madi K, et al. A correlative imaging based methodology for accurate quantitative assessment of bone formation in additive manufactured implants. J Mater Sci Mater Med. 2016;27:112.
202. Palmquist A, Shah FA, Emanuelsson L, Omar O, Suska F. A technique for evaluating bone ingrowth into 3D printed, porous Ti6Al4V implants accurately using X-ray micro-computed tomography and histomorphometry. Micron. 2017;94:1-8.
203. Hara D, Nakashima Y, Sato T, Hirata M, Kanazawa M, Kohno Y, et al. Bone bonding strength of diamond-structured porous titanium-alloy implants manufactured using the electron beam-melting technique. Mater Sci Eng C Mater Biol Appl. 2016;59:1047-52.
204. Thor A, Palmquist A, Hirsch JM, Rannar LE, Derand P, Omar O. Clinical, Morphological, and Molecular Evaluations of Bone Regeneration With an Additive Manufactured Osteosynthesis Plate. J Craniofac Surg. 2016;27:1899-904.
205. Dallas SL, Prideaux M, Bonewald LF. The osteocyte: an endocrine cell ... and more. Endocr Rev. 2013;34:658-90.
206. Kubek DJ, Gattone VH, Allen MR. Methodological assessment of acid-etching for visualizing the osteocyte lacunar-canalicular networks using scanning electron microscopy. Microsc Res Tech. 2010;73:182-6.